Multiple-fault rupture of the *M*7.1 Hector Mine, California, earthquake from fault zone trapped waves

Yong-Gang Li,[1] John E. Vidale,[2] David D. Oglesby,[3] Steven M. Day,[4] and Elizabeth Cochran[2]

Received 12 September 2001; revised 3 July 2002; accepted 9 December 2002; published 25 March 2003.

[1] We studied the complex multiple-faulting pattern of the 40-km-long rupture zone of the 1999 *M*7.1 Hector Mine, California, earthquake with fault zone trapped waves generated by near-surface explosions and aftershocks, and recorded by linear seismic arrays deployed across the surface rupture. The explosion excited trapped waves, with relatively large amplitudes at 3–5 Hz and a long duration of *S* coda waves, are similar to those observed for aftershocks but have lower frequencies and travel more slowly. Three-dimensional finite difference simulations of fault zone trapped waves indicate a 75- to 100-m-wide low-velocity and low-*Q* zone (waveguide) along the rupture surface on the Lavic Lake fault (LLF) in the Bullion Mountains. The *S* velocity within the waveguide varies from 1.0 to 2.5 km/s at depths of 0–8 km, reduced by ~35–45% from the wall rock velocity, and *Q* is ~10–60. The pattern of aftershocks for which we observed trapped waves shows that this low-velocity waveguide has two branches in the northern and southern portions of the rupture zone, indicating a multiple-fault rupture at seismogenic depth. North of the Bullion Mountains, although only the rupture segment on the northwest LLF broke to the surface, a rupture segment on a buried fault also extended ~15 km in the more northerly direction from the main shock epicenter. To the south, the rupture on the LLF intersected the Bullion fault (BF) and bifurcated. The rupture on the south LLF extended ~10 km from the intersection and diminished while there was minor rupture on the southeast BF, which dips to the northeast and disconnects from the LLF at depth. Thus the analysis of fault zone trapped waves helps delineate a more complex set of rupture planes than the surface breakage, in accord with the complex pattern of aftershock distribution and geodetic evidence that the Hector Mine event involved several faults which may also rupture individually. Our simulations of dynamic rupture using a finite element code show that generic models are able to produce the general features of the northern part of the rupture, including slips on subparallel fault segments. The models indicate that such a faulting pattern is physically plausible and consistent with observations. *INDEX TERMS:* 7205 Seismology: Continental crust (1242); 7209 Seismology: Earthquake dynamics and mechanics; 7215 Seismology: Earthquake parameters; 7230 Seismology: Seismicity and seismotectonics; *KEYWORDS:* fault zone trapped waves, fault segmentation and physics, dynamic rupture

Citation: Li, Y.-G., J. E. Vidale, D. D. Oglesby, S. M. Day, and E. Cochran, Multiple-fault rupture of the *M*7.1 Hector Mine, California, earthquake from fault zone trapped waves, *J. Geophys. Res.*, *108*(B3), 2165, doi:10.1029/2001JB001456, 2003.

1. Introduction

[2] The fault zone undergoes violent stressing, shaking, and cracking during an earthquake. Extensive research in the field, in laboratories and with theoretical methods address this phenomenon [*Aki*, 1972; *Kranz and Scholz*, 1977; *Dieterich*, 1978; *Mooney and Ginzburg*, 1986; *Scholz*, 1990; *Rice*, 1992; *Kanamori*, 1994]. Studies have suggested that fault zone complexity helps segment fault zones [*Aki*, 1984; *Schwartz and Coppersmith*, 1984; *Sibson*, 1985; *Wesnousky*, 2000; *Malin et al.*, 1989; *Beck and Christensen*, 1991; *Working Group on California Earthquake Probabilities*, 1995] and control the rhythm of moment release in earthquakes [*Harris and Day*, 1993; *Wald and Heaton*, 1994].

[3] Structural and rheological fault variations, as well as spatial and temporal variations in strength and stress, affect the earthquake rupture [e.g., *Wesson and Ellsworth*, 1973;

[1]Department of Earth Sciences, University of Southern California, Los Angeles, California, USA.
[2]Department of Earth and Space Sciences, University of California, Los Angeles, California, USA.
[3]Department of Earth Sciences, University of Riverside, Riverside, California, USA.
[4]Department of Geological Sciences, San Diego State University, San Diego, California, USA.

0148-0227/03/2001JB001456$09.00

Das and Aki, 1977; *Rice*, 1980; *Day*, 1982; *Vidale et al.*, 1994; *Beroza et al.*, 1995; *Peltzer et al.*, 1998; *Harris and Day*, 1999]. Rupture segmentation is often related to fault bends, step overs, branches, and terminations that have been recognized by surface mapping [e.g., *Sieh et al.*, 1993], exhumation [e.g., *Chester et al.*, 1993], and seismic profiling and tomography [e.g., *Thurber et al.*, 1997; *Lees and Malin*, 1990; *Michelini and McEvilly*, 1991; *Michael and Eberhart-Phillips*, 1991]. Despite these studies, the internal structure of major faults is not well understood, and may hold the key to understanding the physics of earthquakes.

[4] Recently, the fine structure of faults at seismogenic depths has been investigated through fault zone trapped waves [e.g., *Li et al.*, 1990, 1997a, 1997b; *Leary et al.*, 1991; *Hough et al.*, 1994; *Jongmans and Malin*, 1995]. Prominent fault zone trapped waves can be excited by earthquakes and explosions, as long as the sources are located within or close to the fault zone. Since the trapped waves arise from coherent multiple reflections at the boundaries between the low-velocity fault zone and the high-velocity surrounding rock, their amplitudes and frequencies are strongly dependent on the fault geometry and physical properties [*Li*, 1988; *Li and Leary*, 1990; *Li and Vidale*, 1996; *Ben-Zion*, 1998]. Observation and modeling of fault zone trapped waves are able to reveal the fine structure and continuity of the fault zone at depth.

[5] Fault zone trapped waves have been used to study the internal structure and continuity of rupture zones in recent major earthquakes at Landers, California, and Kobe, Japan [*Li et al.*, 1994a, 1994b, 1998b, 1999, 2000]. At Landers, trapped waves generated by aftershocks and near-surface explosions within the rupture zone revealed a ~200-m-wide waveguide, to the seismogenic depths, directly below the surface breaks of the rupture. Within the waveguide, seismic velocities are reduced by ~35–45% from wall rock velocities and Q is 20 to 50. From the viewpoint of fracture mechanics [e.g., *Rice*, 1980; *Papageorgiou and Aki*, 1983; *Cowie and Scholz*, 1992], we interpreted that the trapped wave implied a low-velocity, low-Q zone along the Landers fault zone is partly the transitory result of the dynamic rupture in the 1992 M7.5 earthquake while it probably also represents the accumulated wear from many previous earthquakes. The Landers fault at shallow depth has undergone healing after the main shock [*Li et al.*, 1998a; *Li and Vidale*, 2001], supporting the existence of a broken-then-healing cycle in history of earthquakes on the active faults.

[6] The M7.1 Hector Mine earthquake occurred on 16 October 1999, 30 km east of Landers. This quake had good surface exposure, providing another favorable site for study of fault zone trapped waves. It produced a 40-km-long surface rupture spanning the Lavic Lake fault (LLF) and the Bullion fault (BF) north of the town of Twentynine Palms (Figure 1). This pattern of rupture along multiple mapped faults is similar to that seen in the Landers earthquake. On the LLF in the Bullion Mountains, the faulting has a maximum right-lateral strike slip of 5 m and is relatively simple, with most of the surface slip on a single trace or closely spaced parallel traces. In contrast, the southern and northern portions of the rupture zone had a more complex faulting pattern with minor slips [*Scientists from USGS, SCEC, and CDMG*, 2000].

[7] Immediately after the main shock, we deployed portable seismographs in dense linear arrays across the LLF in the Bullion Mountains and the BF in Bullion Wash. Our deployment was coordinated by the U.S. Geological Survey and organized by the Southern California Earthquake Center (SCEC), with the cooperation and assistance of the Marine Corps Air Ground Combat Center (MCAGCC), Twentynine Palms, California. We recorded 4–7 Hz fault zone trapped waves at the northern array in the Bullion Mountains for aftershocks occurring within the rupture zone [*Li et al.*, 2002]. These trapped waves have higher frequencies but are otherwise similar to those observed at the Landers rupture zone in 1992, suggesting a narrower rupture zone in the Hector Mine earthquake than that in the Landers earthquake. Comparison of the records with three-dimensional (3-D) finite difference simulations of trapped waves from the Hector Mine aftershocks indicates a 75- to 100-m-wide low-velocity and low-Q waveguide along the rupture zone in which the S velocity is reduced by ~35–45% from wall rock velocities, and Q is ~10–60 in the depth range from the surface to ~10 km. We interpret this low-velocity waveguide as marking the process zone (break-down zone) of the dynamic rupture in the 1999 Hector Mine earthquake. Locations of aftershocks showing trapped waves delineate a more complex set of rupture planes with bifurcation in the northern and southern portions of the rupture zone at seismogenic depths than the surface breakage. Preliminary dynamic simulations indicate that models with a bifurcated rupture zone are physically plausible.

2. Field Experiment

[8] In order to study shallow fault zone structure and detect healing of the Hector Mine rupture zone with time if it occurs, we detonated explosions within the rupture zone in the Fall of 2000. The signals from explosions were recorded at three tight linear seismic arrays deployed across the rupture zone in the Bullion Mountains and Quackenbush (Figure 1). We use explosion-excited trapped waves to document the shallow rupture zone to a depth of a few kilometers. This is useful for stripping shallow effects to resolve internal fault zone structure deeper, in the seismogenic zone. The arrays also recorded aftershocks for several weeks. The signals from aftershocks were used to delineate the deep structure of fault zone.

[9] Figure 1 shows locations of the arrays, shot holes, and aftershocks. Array 1 was composed of 18 three-component stations along a 350-m-long line across the north LLF in the Bullion Mountains. The LLF experienced 4-m right-lateral slip at the array site, ~6 km south of the 1999 M7.1 Hector Mine earthquake epicenter, where the rupture zone is ~70 m wide, including one major and several parallel minor faults at the surface in the main shock. Arrays 2 and 3 were 500 m long and composed of 20 and 19 stations, respectively. These two arrays were located ~18 km south of the main shock epicenter and across the south LLF and southeast BF, ~1 km apart from each other. The lateral slips were <1 m at array sites. Vertical slips were 0.3–0.5 m, with the west side up at site array 2, but with the east side up at site array 3. Station spacing in the array was not even, with 12.5-m separation for nine stations close

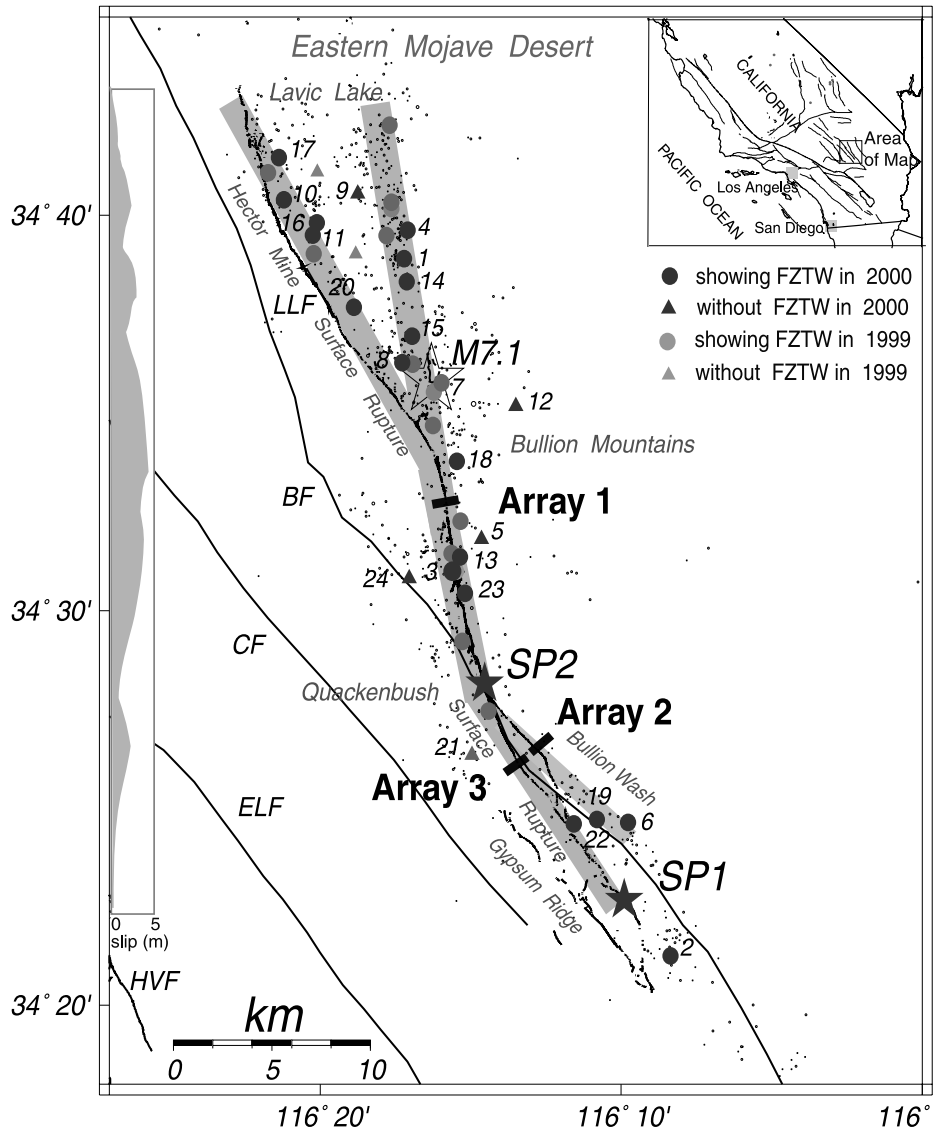

Figure 1. Map of the survey area showing locations of seismic arrays (arrays 1, 2, and 3) deployed across the rupture zone of the 1999 *M*7.1 Hector Mine earthquake and explosions SP1 and SP2 detonated within the rupture zone. Solid circles and triangles with numbers denote epicenters of aftershocks recorded in 2000, which waveform data are shown in this paper. Shaded circles and triangles denote aftershocks recorded in 1999, which waveforms have been shown in another paper [*Li et al.*, 2002]. Circles denote events showing fault zone trapped waves (FZTW), while triangles denote events without FZTW. Dots denote aftershocks occurred in November 1999 and in September 2000. BF, Bullion fault; CF, Calico Fault; ELF, Emerson Lake fault; HVF, Homestead Valley fault; JVF, Johnson Valley fault; LLF, Lavic Lake fault. Surface ruptures along the LLF and southeast BF are denoted. The shaded fault segments are the trapped wave inferred rupture zone of the 1999 Hector Mine earthquake. The right-lateral slip profile on the LLF [*Scientists from USGS, SCEC, and CDMG*, 2000] is shown at left of the rupture zone. The inset shows the location of the area of map.

to the main fault trace and 25- or 50-m spacing for farther stations. Station ST0, at the center of each array, was deployed on the main fault trace. The coordinates of station ST0 were 34°N31.05′ and 116°W15.71′ in array 1, 34°N26.31′ and 116°W12.56′ in array 2, and 34°N25.91′ and 116°W13.21′ in array 3.

[10] Two shots were detonated in 40-m-deep shot holes drilled in the rupture zone at sites SP1 and SP2 located ~12.5 and ~25 km south of the main shock epicenter, respectively. SP2 was close to the southern edge of the Bullion Mountains where the LLF had 1.5–2.0 m slip at surface in the main shock. SP1 was close to the south end of rupture zone near Gypsum Ridge, where surface slips were <0.5 m. The shot holes required casing because of a soft weathering layer at the drilling sites. Each shot hole was loaded with 1000 pounds of chemical emulsions. The coordinates of shot holes are shown in Table 1. The fault lines and surface displacements at seismic array and shot

Table 1. Times and Locations of Hector Mine Aftershocks Which Seismograms are Shown in Figures

Event	Julian Day	Date	Origin Time, UT	Latitude, N	Longitude, W	Depth, km	Magnitude
1	254	10 Sept. 2000	1946:17.61	34°38.91′	116°17.21′	5.25	2.3
2	254	10 Sept. 2000	2313:57.29	34°21.26′	116°08.36′	6.99	1.4
3	255	11 Sept. 2000	0806:42.80	34°31.00′	116°16.36′	11.68	1.2
4	255	11 Sept. 2000	0935:59.93	34°39.63′	116°17.05′	8.52	2.1
5	255	11 Sept. 2000	1725:40.48	34°31.81′	116°14.66′	11.00	1.5
6	255	11 Sept. 2000	1857:43.12	34°24.61′	116°09.76′	7.36	1.6
7	256	12 Sept. 2000	0341:17.19	34°35.65′	116°15.84′	4.46	1.7
8	256	12 Sept. 2000	0657:02.16	34°36.28′	116°17.26′	6.00	1.6
9	256	12 Sept. 2000	1850:56.33	34°40.54′	116°18.75′	1.90	1.5
10	257	13 Sept. 2000	0650:41.99	34°40.39′	116°21.20′	2.73	1.3
11	257	13 Sept. 2000	1450:52.81	34°39.50′	116°20.24′	3.23	1.9
12	258	14 Sept. 2000	1504:27.00	34°35.17′	116°13.50′	4.36	1.7
13	258	14 Sept. 2000	1705:56.56	34°31.36′	116°15.25′	7.64	1.6
14	259	15 Sept. 2000	1150:20.74	34°38.33′	116°17.12′	6.07	1.5
15	259	15 Sept. 2000	1413:29.26	34°36.95′	116°17.11′	10.00	1.9
16	259	15 Sept. 2000	1654:19.06	34°39.81′	116°19.77′	5.12	1.6
17	259	15 Sept. 2000	1712:21.20	34°41.46′	116°21.36′	8.21	1.8
18	259	15 Sept. 2000	2322:15.41	34°33.62′	116°15.33′	11.40	1.4
19	260	16 Sept. 2000	0115:10.66	34°24.72′	116°11.00′	5.70	1.6
20	260	16 Sept. 2000	1553:14.85	34°37.68′	116°18.87′	3.83	1.5
21	261	17 Sept. 2000	1302:03.52	34°26.34′	116°14.95′	7.61	1.6
22	262	18 Sept. 2000	1045:00.31	34°24.60′	116°11.57′	5.18	1.5
23	263	19 Sept. 2000	0926:55.47	34°30.45′	116°15.06′	2.95	1.3
24	264	20 Sept. 2000	2359:21.80	34°30.81′	116°17.41′	6.00	1.3
SP1	297	23 Oct. 2000	1430:00.00	34°22.49′	116°09.73′	0.04	SP1
SP2	297	23 Oct. 2000	1530:00.00	34°27.74′	116°14.77′	0.04	SP2

hole sites were well mapped [*Scientists from the USGS, SCEC, and CDMG*, 2000].

[11] We used three-channel REFTEK recorders and three-component sensors (Mark Products 2 Hz L22) from the PASSCAL Instrument Center of Incorporated Research Institutions for Seismology (IRIS). The three components of the sensor at each station were aligned vertical, parallel, and perpendicular to the fault trace. Sensors were buried to minimize wind noise and improve coupling. REFTEKs were set in trigger mode to record aftershocks and in timing mode to record explosions. The signals were recorded at a rate of 100 samples per second for aftershocks and 1000 samples per second for explosions. The clocks of all recorders and explosions were synchronized through Global Positioning System (GPS). The timing errors for recorders and explosions were <0.001 s.

3. Trapped Waves Generated by Explosions

[12] Figure 2 demonstrates the fault zone trapped waves generated by explosions. Figure 2a shows three-component seismograms recorded at array 1 across the surface rupture on the LLF in the Bullion Mountains for shot SP2 located ~7.5 km south of the array. *P* and *S* waves arrive at 2.2 s and 4.5 s after the origin time of shot. Trapped waves with relatively large amplitudes following *S* waves appeared at stations between E3 and W4, close to the fault trace. The distance between stations E3 and W4 is 87.5 m, in which the main fault trace and several subfault traces expose at the surface. We note that trapped waves are dominant between 4.5 and 6 s but continue until 9 s, showing multiple trapped wave trains. Trapped waves are shown more clear in the fault-parallel component than in other two components. In contrast, trapped waves are not clear at stations farther away from the fault trace. We interpret that these trapped waves are formed due to the waveguide effect of the low velocity of the rupture zone. On the basis of the distance between stations E3 and W4 in which prominent trapped waves are exhibited, we estimate that the width of rupture zone (waveguide) on the north LLF at site of array 1 is 75–100 m.

[13] The coda-normalized amplitude spectra of seismograms for a 3-s time window starting from the *S* arrivals show a maximum at ~3 Hz at stations close to the main fault trace (Figure 2b). These spectra were normalized using coda waves to eliminate instrument, site and source effects on the spectral amplitudes of trapped waves as we did for analyses of trapped waves recorded at the Landers rupture zone [*Li et al.*, 1994a]. The dominant frequency of explosion-excited trapped waves recorded at the Hector Mine rupture zone is higher than that (~2 Hz) observed for explosions at the Landers rupture zone [*Li et al.*, 1999], indicating a narrower or a higher speed waveguide on the Hector Mine rupture zone.

[14] Figure 2c shows the trapped waves recorded at array 1 for shot SP1 detonated within the southernmost part of the Hector Mine rupture zone at a distance of ~20 km from the array. *P* and *S* waves arrive at ~5 and ~10 s, respectively. Fault zone trapped waves are prominent at stations between E3 and W4 within the rupture zone. Again, we observe multiple wave trains of trapped waves; the early wave train appears between 11 and 13 s, while the late wave train appear between 14 and 17 s. We interpret that the early trapped wave train traversed the deep part of the rupture zone, while the late trapped wave train traveled in the shallow rupture zone with lower velocity. Coda-normalized amplitude spectra of the early trapped waves show a maximum peak at ~3 Hz, which decreases with station offset from the rupture zone.

[15] The separation between the *S* wave and the dominant trapped wave in the early trapped wave train is ~1.5 s for SP2 and ~3 s for SP1. The separation increases with the distance between the array and shots along the rupture zone, showing that trapped waves were formed within a roughly continuous low-velocity waveguide along the rupture zone between the shots and array but not caused by a local low-velocity structure at the array site. However, the increase in

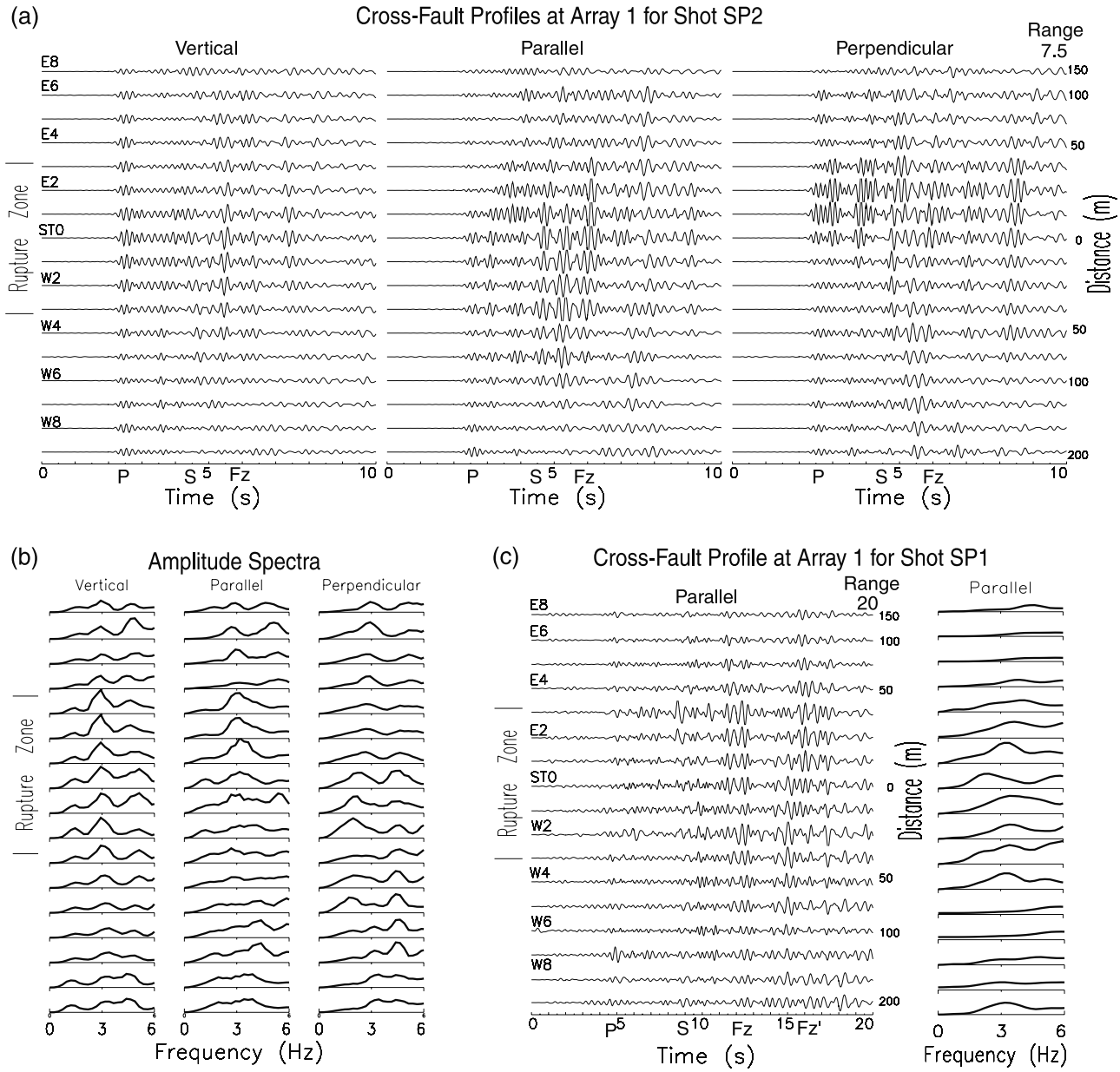

Figure 2. (a) Vertical, parallel-to-fault and perpendicular-to-fault seismograms recorded at north array 1 across the surface rupture on the Lavic Lake fault in Bullion Mountains for explosion SP2 detonated within the rupture zone 7.5 km (range) south of the array. Station ST0 of the array was located on the main fault trace. The distances of other stations from the fault trace are plotted at right to profiles. Station names initiated by E or W denote the station located at the east or west side, respectively, of the fault trace. Station E7 was dead due to battery exhausted. The recorded seismograms were deconvoluted by the sensor and instrument response in situ. Seismograms have been band-pass-filtered (2–6 Hz) and plotted using a fixed amplitude scale for all traces in three-component profiles. Fault zone (Fz) trapped waves with large amplitudes and long duration appear between 4.5 s and 9 s at stations between E3 and W4. Solid bars mark the rupture zone width inferred by trapped waves, within which one major and several minor faults were seen at this site. (b) Coda-normalized amplitude spectra of trapped waves at array 1 for shot SP2 are plotted using a fixed amplitude scale of 150. Trapped waves in a time window with 3-s length starting from *S* arrivals were used in computation (1000 samples for Fourier transformation) using a Hanning window with a 60-ms taper). The amplitude spectra of coda waves were calculated in a time window with the same length starting at 35 s after the explosion time. Spectral amplitudes show a maximum peak at ~3 at stations within or close to the rupture zone. (c) (left) Parallel-to-fault component seismograms at array 1 for shot SP1 detonated at ~20 km south of the array. Seismograms have been low pass filtered (<4 Hz). Fault zone trapped waves appeared between 10 and 18 s. (right) Coda-normalized amplitude spectra of trapped waves are plotted using a fixed amplitude scale of 30. The spectral amplitudes show a maximum peak at ~3 Hz at stations within the rupture zone. Other notations are the same as in Figure 2.

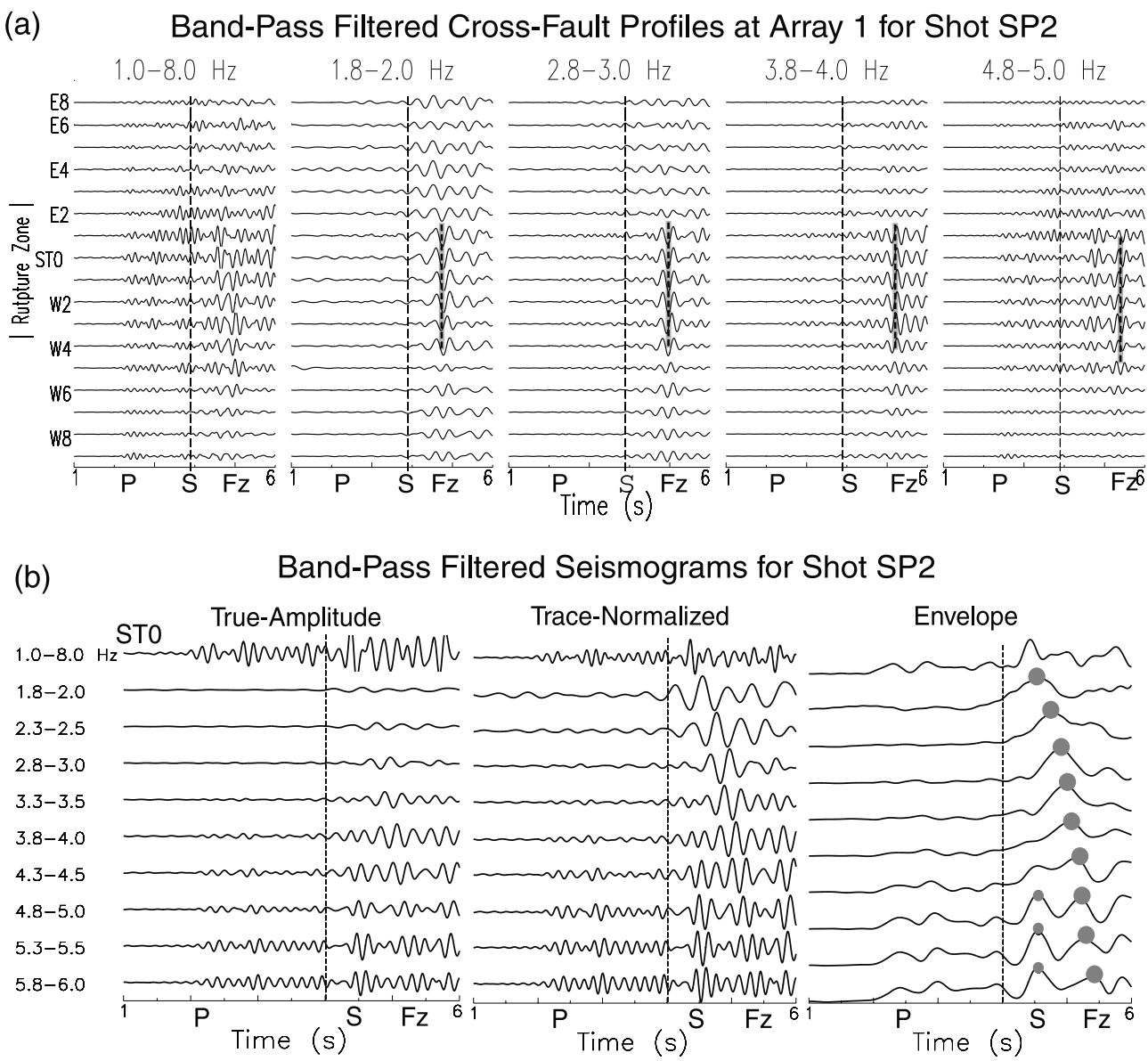

Figure 3. (a) Band-pass-filtered parallel-to-fault component seismograms at array 1 for shot SP2 in 5 frequency bands. Vertical dashed lines align with the *S* arrivals. Grey bars denote the dominant trapped waves with large amplitudes. Trapped waves at lower frequencies travel faster than those at higher frequencies. (b) Parallel-to-fault component seismograms at station ST0 of array 1 for SP2 are filtered in nine frequency bands between 1.8 and 6.0 Hz. Multiple band-pass-filtered seismograms are plotted using (left) a fixed amplitude scale for all traces and (middle) peak-to-peak amplitude for each trace. Computed envelopes of filtered seismograms in the trace-normalized profile are plotted at right. The peak of envelope marked by a grey circle denotes the arrival of energy at the specified frequency band. Small shaded circles denote the amplitudes of *S* waves.

Figure 4. (opposite) (a) Three-component seismograms recorded at array 3 across the south LLF for shot SP2 located ~4.5 km north of the array. Seismograms have been band-pass-filtered (2–6 Hz) and plotted using a fixed amplitude scale for all traces. Station ST0 was located on the fault trace. Stations E3 and W1 were skipped due to the road path, while station W4 was dead during explosions. *P* and *S* waves arrive at 1.8 and 3.5 s. Fault zone trapped waves with large amplitudes and long duration appear between 4 and 10 s at stations between ST0 and W8. Fz and Fz' denote the early and late wave trains of trapped waves. (b) Coda-normalized amplitude spectra of trapped waves at array 3 for shot SP2. Trapped waves in two time windows 4–7 s and 7–10 s are plotted using a fixed amplitude of 600 and 800, respectively. Other notations are the same as in Figure 2. (c) Parallel-to-fault component seismograms at station W3 of array 3 for SP2 are filtered in 9 frequency bands between 1.8 and 6.0 Hz. Multiple band-pass-filtered seismograms are plotted in true amplitude and in trace-normalized profile for two time windows between 0 and 5 s and between 2 and 7 s. The peak of computed envelope marked by a shaded circle denotes the arrival of fault zone (Fz) trapped wave energy at the specified frequency band. Small shaded circles denote *S* arrivals. Other notations are the same as in Figure 3.

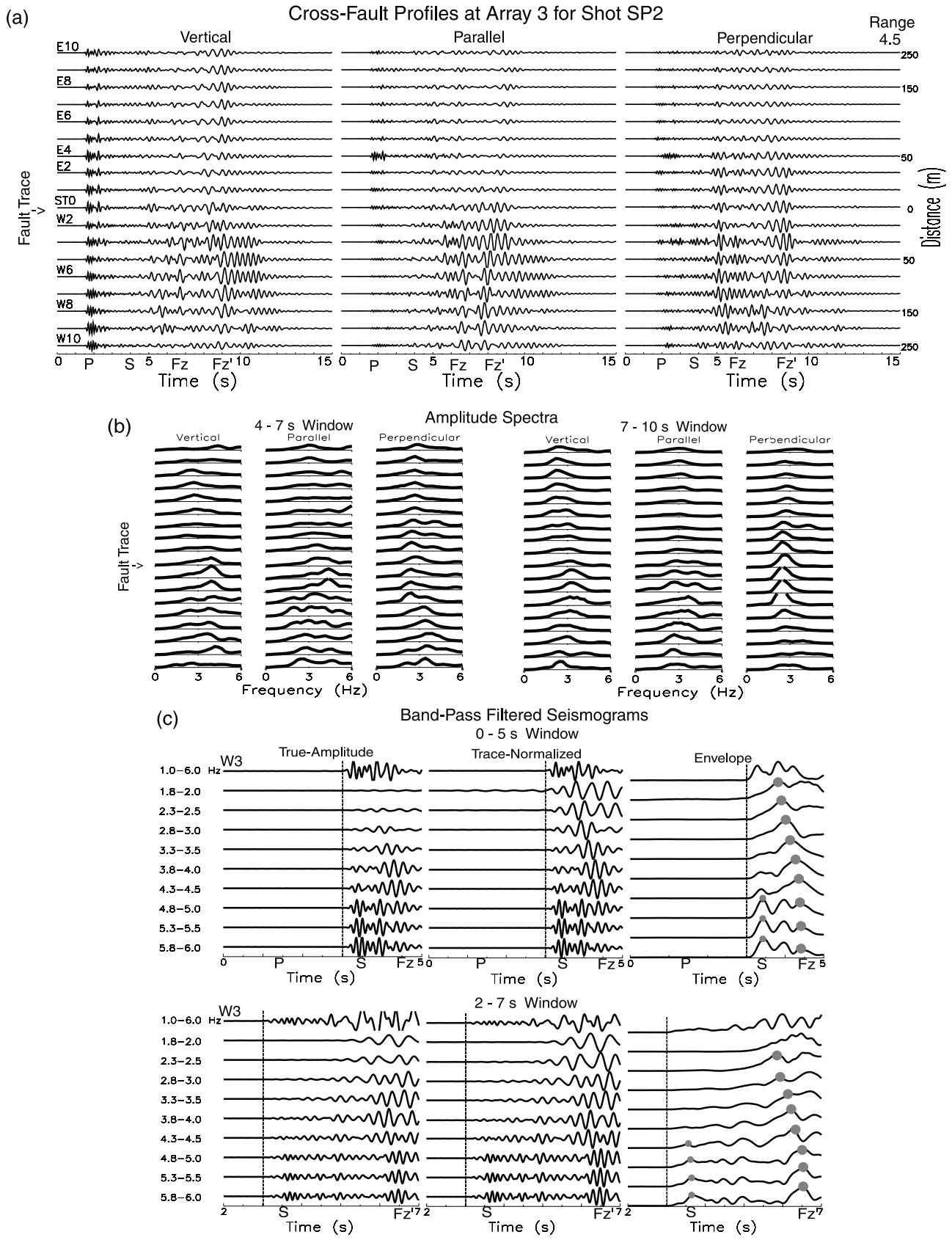
(a)
Cross-Fault Profiles at Array 3 for Shot SP2
Vertical
Parallel
Perpendicular
Range
4.5
E10
E8
E6
E4
E2
STO
W2
W6
W8
W10
Fault Trace
250
150
50
0
50
150
250
Distance (m)
P
S
Fz
Fz'
Time (s)
(b)
Amplitude Spectra
4 - 7 s Window
7 - 10 s Window
Vertical
Parallel
Perpendicular
Fault Trace
Frequency (Hz)
(c)
Band-Pass Filtered Seismograms
0 - 5 s Window
2 - 7 s Window
True-Amplitude
Trace-Normalized
Envelope
W3
1.0–6.0 Hz
1.8–2.0
2.3–2.5
2.8–3.0
3.3–3.5
3.8–4.0
4.3–4.5
4.8–5.0
5.3–5.5
5.8–6.0
Time (s)

delay time of trapped waves is not linearly proportional to the increase of the travel distance since waves from farther shot SP1 penetrated the deeper part of the rupture zone with higher velocities.

[16] In order to examine the dispersion of the trapped waves, we filtered the seismograms using multiple band-pass filters. We applied a four-pole Butterworth filter with 0.2 Hz passband. For example, Figure 3a shows filtered seismograms in cross-fault profile at array 1 for shot SP2 in 5 frequency bands: 1.0–8.0 Hz, 1.8–2.0 Hz, 2.8–3.0 Hz, 3.8–4.0 Hz, and 4.8–5.0 Hz. Trapped waves at lower frequencies travel faster than those at higher frequencies. The seismic energy at higher frequencies is more concentrated within the rupture zone. Because of this dispersion and concentration of fault zone trapped waves in and near the rupture zone, these waves can be used to probe the internal structure of the rupture zone.

[17] Figure 3b shows multiple band-pass-filtered seismograms at station ST0 of array 1 for SP2 in 9 frequency bands between 1.8 and 6.0 Hz. Station ST0 was located within the rupture zone. We also computed the envelope of filtered seismograms using a Hilbert transformation. The peak in the envelope indicates the arrival of energy in the specified frequency band. The filtered seismograms in the true-amplitude profile show dominant trapped waves at 3.3–4.5 Hz. Trapped waves at higher frequencies travel slower than those at lower frequencies, showing the dispersion of trapped waves. In contrast, *S* waves at 4.5–6.0 Hz are without dispersion. From multiple band-pass-filtered seismograms at stations located within the rupture zone, we measured group velocities of trapped waves for shot SP2, ranging from ~1.7 km/s at 1.8 Hz to ~1.3 km/s at 6 Hz. Similarly, we measured group velocities of trapped waves for SP1, ranging from ~2.0 km/s at 1.8 Hz to ~1.5 km/s at 6 Hz. The measured group velocities were used as velocity constraints in modeling trapped waves.

[18] Prominent fault zone trapped waves were recorded at array 3 across the south LLF in Quakenbush. Figure 4a illustrates three-component seismograms at array 3 for shot SP2. The distance between the shot and array was ~4.5 km. At this site, a soft-sand wash zone passes the east part of the array between stations E2 and E7. We anticipated strong surface waves to appear at these stations. However, we observed the wave trains with large amplitude and long duration after *S* arrivals at stations between ST0 and W8 on the west part of the array. These wave trains are interpreted as the guided waves trapped within the low-velocity rupture zone which passes the west part of the array. Trapped waves appear between 4 and 10 s with multiple wave trains, suggesting a vertical velocity gradient within the rupture zone. We note that waves traveled from SP2 to array 3 in Quackenbush sediments more slowly than they traveled to array 1 in the Bullion Mountains. The great time delay of the late trapped energy after *S* waves indicates a very low velocity of the rupture zone at shallow depth in Quackenbush.

[19] Coda-normalized amplitude spectra of seismograms in two time windows (4–7 s and 7–10 s) covering the early and late trapped wave trains, respectively, are shown in Figure 4b. The normalized spectra show large amplitudes of trapped waves at 3–5 Hz at stations between ST0 and W8 of the array. Figure 4c shows multiple band-pass seismograms at station W3 in nine frequency bands between 1.8 and 6.0 Hz and envelopes of filtered seismograms in two time windows. The time window 0–5 s covers the earliest trapped wave train following *S* waves, and the time window 2–7 s includes the late trapped wave train. The early trapped wave train traversed the deeper rupture zone while the late trapped wave train traveled in the shallow part of the rupture zone. Trapped waves at higher frequencies traveled more slowly than those at lower frequencies, showing the dispersion, while *S* waves show without dispersion. Trapped waves in the true-amplitude profile are dominant at 3.5–4.5 Hz. We measured group velocities of the earliest trapped wave train at array 3 for shot SP2, ranging from ~1.5 km/s at 1 Hz to ~1.0 km/s at 4.5 Hz. Similarly, group velocities of the late trapped wave train, ranging from ~1.0 km/s at 1 Hz to ~0.7 km/s at 4.5 Hz, indicating very low velocities in the sediments at Quakenbush.

[20] However, fault zone trapped waves did not appear clearly at array 2 across the southeast BF although the slips of ~0.5–1.0 m exposed at this site in the 1999 main shock. Station ST0 of array 2 was located on the surface rupture. The west part of array was on a hill of sedimentary rock while the east part of array was in the soft-sand Bullion wash. Figure 5a shows seismograms at array 2 for shot SP2. We observed wave trains with relatively large amplitudes after *S* waves at stations near the east end of the array but not at stations close to the rupture trace. Those wave trains were surface waves traveling in Bullion Wash. The fault zone trapped waves, if they formed on the BF, might have been affected by the soft-sand wash zone abutting to the fault on the east side.

[21] Figure 5b shows seismograms recorded at arrays 2 and 3 for shot SP1 detonated at the south end of the rupture zone on the LLF, ~8 km south of two arrays. We observed fault zone trapped waves clearly at array 3 across the LLF but not at array 2 across the BF. Trapped waves arrived at array 3 between 14 and 16 s. The separations between *S* waves and trapped waves from SP1 and SP2 to array 3 are roughly proportional to the distance between the shots and array, showing a low-velocity waveguide on the southern part of the LLF. On the other hand, no clear trapped waves were recorded at array 2 either for SP1 or SP2, showing that the low-velocity waveguide on the southeast BF was not

Figure 5. (opposite) (a) Vertical and parallel-to-fault seismograms at array 2 at array 2 across the southeast BF for shot SP2 detonated ~4.5 km north of the array. Seismograms have been band pass filtered (2–6 Hz) and plotted using a fixed amplitude scale same as in Figure 4a for all traces. Station ST0 was located at the fault trace. Stations E9 and W2 were dead due to battery exhausted. (b) Vertical and parallel-to-fault seismograms at array 2 across the BF and array 3 across the LLF for shot SP2 detonated at ~8 km south of two arrays. Seismograms have been low pass filtered (<5 Hz) and plotted using a fixed amplitude scale for all traces of profiles at two arrays. Fault zone trapped waves with large amplitudes and long-duration after *S* waves appear between 13 and 17 s at stations between ST0 and W8 of array 3 but not at array 2. Other notations are the same as in Figures 2 and 4.

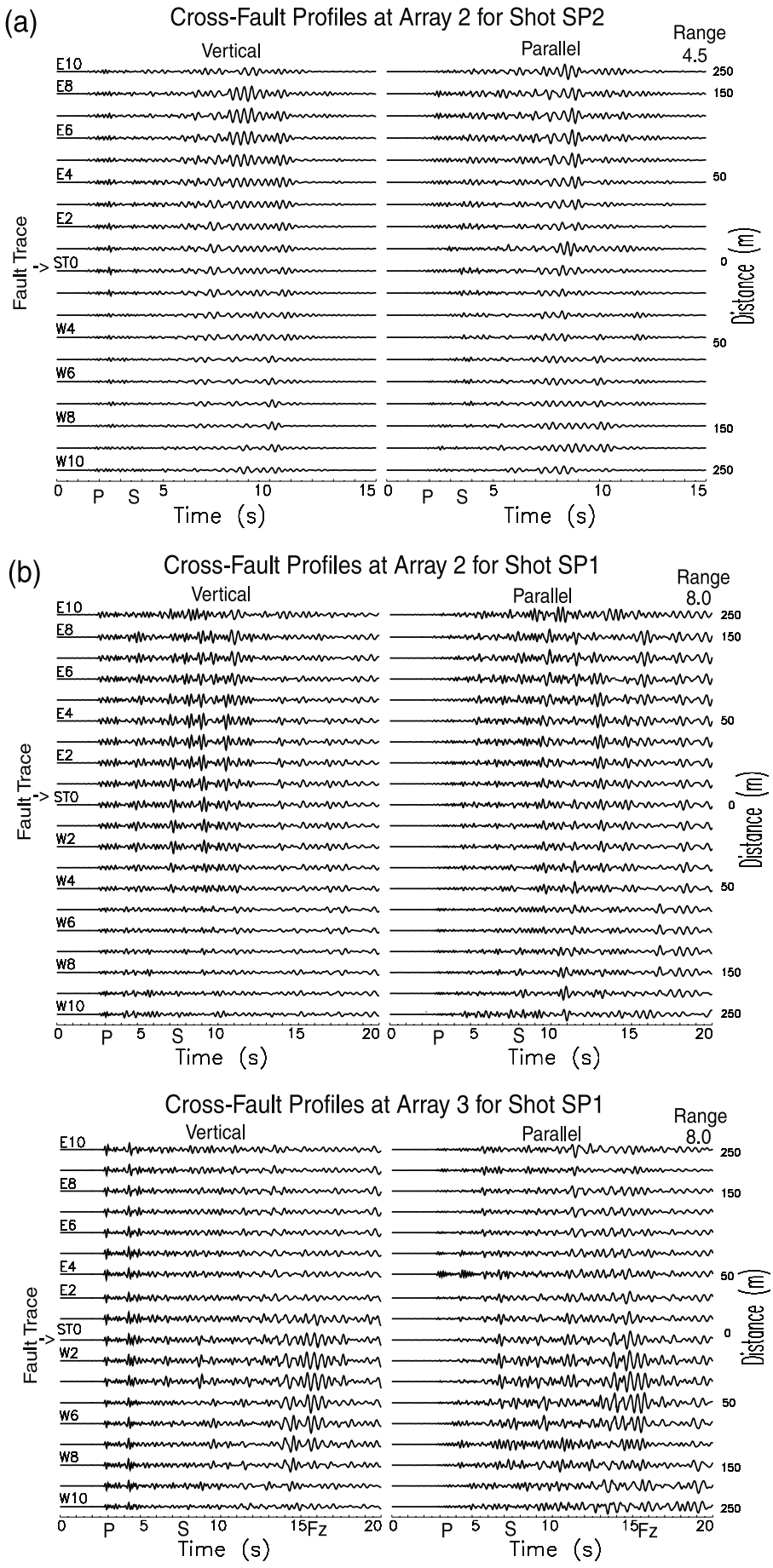
(a)
Cross-Fault Profiles at Array 2 for Shot SP2
Vertical
Parallel
Range
4.5
E10
E8
E6
E4
E2
ST0
W4
W6
W8
W10
Fault Trace
Distance (m)
250
150
50
0
50
150
250
P
S
Time (s)
(b)
Cross-Fault Profiles at Array 2 for Shot SP1
Vertical
Parallel
Range
8.0
E10
E8
E6
E4
E2
ST0
W2
W4
W6
W8
W10
Fault Trace
Distance (m)
Time (s)
Cross-Fault Profiles at Array 3 for Shot SP1
Vertical
Parallel
Range
8.0
E10
E8
E6
E4
E2
ST0
W2
W6
W8
W10
Fault Trace
Distance (m)
Fz
Time (s)

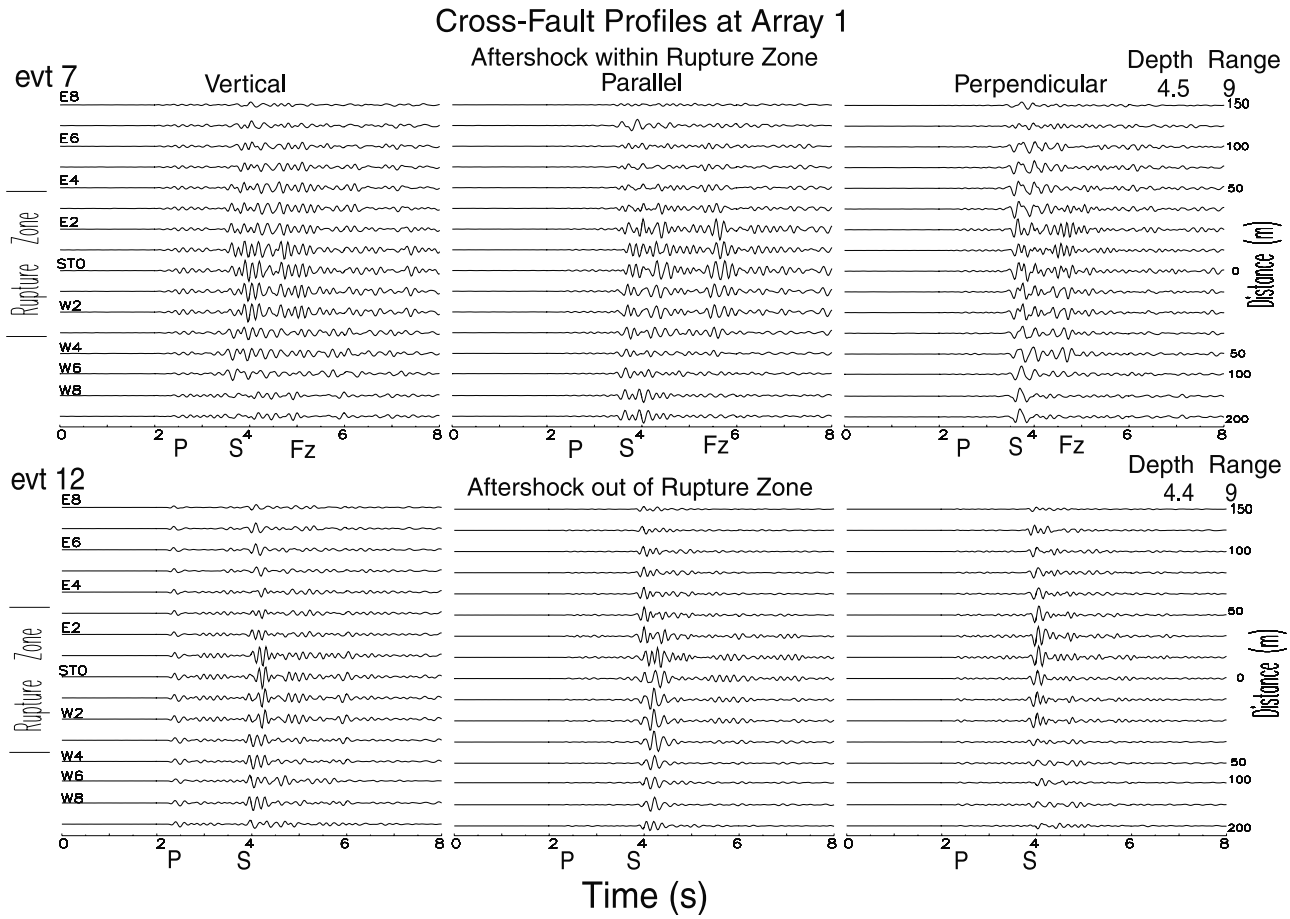

Figure 6. Three-component seismograms recorded at array 1 for two aftershocks (events 7 and 12 in Figure 1 and Table 1). Event 7 occurred within the Hector Mine northern rupture zone, while event 12 occurred 5 km east of the rupture zone. The depths and hypocentral distances (range in km) of these two events shown at the top right of each plot are almost the same. Seismograms have been low pass filtered (<7 Hz) and are plotted using a fixed amplitude scale in each profile. Trapped waves (Fz) are prominent at stations between E2 and W4 for event 7, but not clear for event 12. Stations E3, W5, and W7 were not triggered by the events. Other notations are the same as in Figure 2.

well developed even though there were minor slips on it in the 1999 earthquake, and the southeast BF disconnects from the LLF at depth.

4. Trapped Waves From Aftershocks

[22] We used trapped waves generated by aftershocks to further study the geometry and properties of the Hector Mine rupture zone at seismogenic depth. During the first 10 days of our field experiment between 10 and 20 September 2000, we recorded ~150 events at portable arrays. About 25 aftershocks among them show fault zone trapped waves. In this paper, we display waveforms of 24 aftershocks with and without prominent trapped waves, whose location and times are shown in Table 1.

[23] Figure 6 shows three-component seismograms recorded at array 1 across the north LLF for three aftershocks (events 7 and 12 in Figure 1 and Table 1). Event 7

Figure 7. (opposite) (a) Vertical component seismograms at array 1 for four aftershocks (events 3, 5, 13, and 23 in Figure 1 and Table 1) located south of the array. Trapped waves are prominent at stations close to the LLF for events 3, 13, and 23 occurring within the rupture zone but are not clear for event 5 occurring ~1.5 km east of the rupture zone. Vertical dashed lines align with the *S* arrivals. Shaded bars denote the dominant trapped waves with large amplitudes. The separation between *S* and trapped waves increases with hypocentral distance of events 23, 13, and 3. Other notations are the same as in Figure 6. (b) Parallel-to-fault component seismograms at station ST0 of array 1 for events 3, 5, 13, and 23 are filtered in nine frequency bands between 3.3 and 7.5 Hz. Multiple band-pass-filtered seismograms are plotted in the trace-normalized profile. Computed envelopes of filtered seismograms are plotted at right. The peak of envelope marked by a shaded circle denotes the arrival of trapped energy at the specified frequency band. Trapped waves at higher frequencies are slower than those at lower frequencies, showing dispersion of trapped waves. Small shaded circles denote the amplitudes of *S* waves, showing without dispersion. Other notations are the same as in Figure 3.

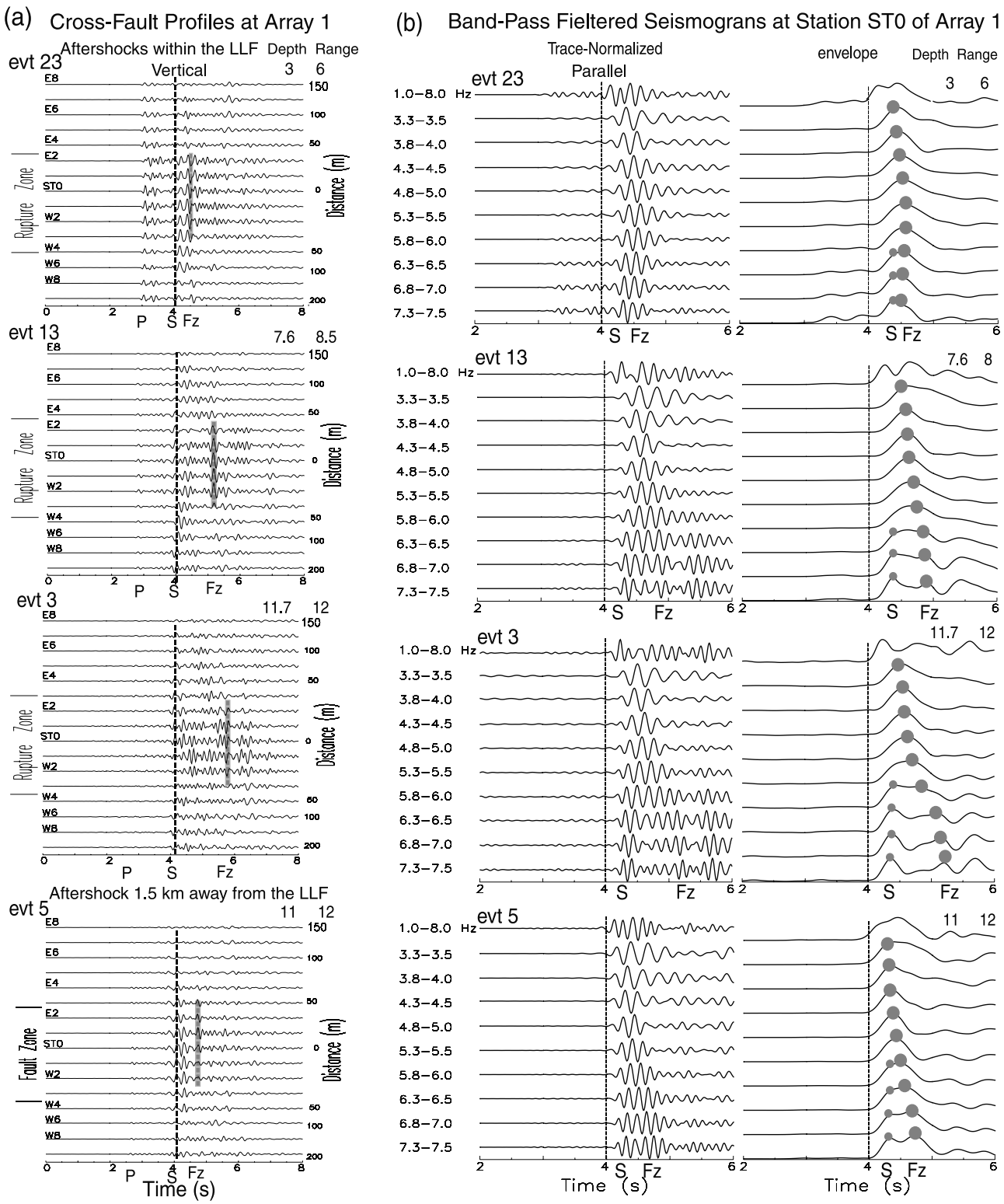

occurred at the depth of 4.5 km within the rupture zone near the main shock epicenter. We observed prominent fault zone trapped waves with relatively large amplitudes and long duration after *S* waves at stations between E3 and W4 located close to the trace of the LLF. These trapped waves are similar to those recorded on the north LLF in the Bullion Mountains in our previous experiment [*Li et al.*, 2002]. The dominant frequencies of trapped waves generated by aftershocks are 4–7 Hz, higher than those from explosions, indicating that the higher velocities within the deeper part of the low-velocity waveguide, and the waveguide is probably narrower at depth than near surface. We note that the duration of trapped wave trains after *S* waves in three components are not the same, probably due to the anisotropy of fault zone rock. In contrast, trapped waves were not clear at the same array for event 12 occurring ~5 km east of

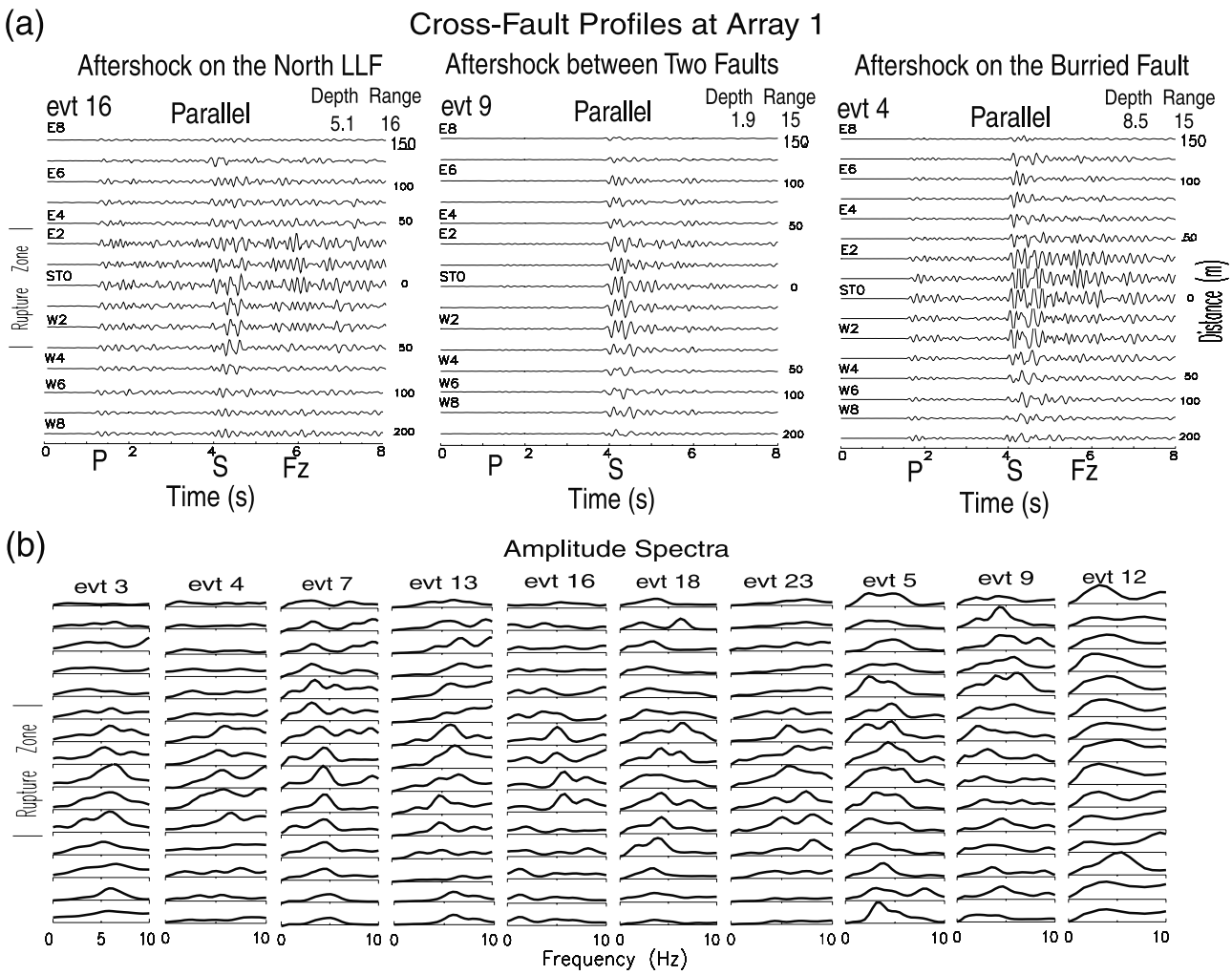

Figure 8. (a) Parallel-to-fault component seismograms recorded at array 1 for three aftershocks occurring north of the main shock epicenter. Events 16 and 4 occurred on the north LLF and the buried fault, respectively. Event 9 occurred between them. Trapped waves are prominent at stations close to the fault trace for events 4 and 16, but not for event 9. (b) Computed amplitude spectral ratios of trapped waves to *P* waves at array 1 for 10 aftershocks. Events 3, 4, 7, 13, 16, 18, and 23 occurred within the rupture zone, while events 5, 9, and 12 occurred away from the rupture zone. The spectral ratios in each panel are normalized to the maximum peak amplitude and are plotted using a unit amplitude scale for all stations.

the LLF because it was located too far away from the rupture zone to generate fault zone guided waves. In this and our previous studies either for observations [e.g., *Li et al.*, 1990, 1994a] or for synthetic seismograms [e.g., *Li and Leary*, 1990; *Li and Vidale*, 1996], events far from the fault segment on which the array is located generally do not excite prominent fault zone guided waves. In contrast, events near the fault often but not always excite guided waves, perhaps due to strong variation of structure along the fault zone.

[24] Figure 7 shows seismograms at array 1 for other four aftershocks (events 3, 5, 13, and 23 in Figure 1 and Table 1) located 3–5 km south of array 1. Events 3, 13, and 23 occurred on the LLF at depths of 3, 7.6, and 11.7 km, respectively. Prominent fault zone trapped waves were recorded at stations close to the LLF trace. The duration of trapped wave trains after *S* waves from these aftershocks increases with hypocentral distance, indicating a roughly continuous low-velocity waveguide on the LLF to ~11 km depth. However, the wave train following *S* wave from event 5, which occurred ~1.5 km away from the LLF and shows little trapped waves with much a shorter duration than that for event 3, although the two events were located at the similar depth and hypocentral distances. Multiple band-pass-filtered seismograms and envelopes in nine frequency bands between 3.3 and 7.5 Hz at station ST0 for these aftershocks show that trapped waves at higher frequencies are slower than those at lower frequencies, illuminating the dispersion of trapped waves. However, *S* waves show without dispersion. From band-pass-filtered seismograms, we measured group velocities of trapped waves. They range from ~2.3 km/s at 3.3 Hz to ~1.8 km/s at 6 Hz for event 23, from ~2.7 km/s at 3.3 Hz to 2.0 km/s at 6 Hz for event 13, and from ~3.0 km/s at 3.3 Hz to 2.4 km/s at

6 Hz for event 3, showing a depth-dependent velocity structure within the rupture zone. These group velocities are used as velocity constraints in numerical modeling of fault zone trapped waves.

[25] We then examined the waveform data for aftershocks located north of the main shock epicenter. We found that there were two groups of aftershocks generating fault zone trapped waves. Events in the first group occurred on the north LLF while events in the second group occurred on a line with more northerly direction from the main shock epicenter. For example, Figure 8a show seismograms recorded at array 1 for three aftershocks (events 16, 4, and 9 in Figure 1) located at the similar hypocentral distances north of the array. Events 16, 4, and 9 occurred on the north LLF, the northerly directing line, and between them, respectively. We observed dominant fault zone trapped waves with large amplitudes and long time duration after *S* waves for events 16 and 4 but not for event 9, indicating the existence of low-velocity waveguides on the north LLF and also on the more northerly directing line. Because the aftershocks which occurred north of the main shock epicenter and showed trapped waves were located either on the north LLF or on the more northerly line (Figure 1), we speculate that there exists a buried fault along the northerly directing line. The existence of this blind fault will be shown later.

[26] In order to eliminate the site on trapped waves in waveform analysis, we computed the spectral ratio of fault zone trapped waves to *P* waves for those aftershocks. The amplitude spectra of trapped waves computed in a 2-s time window after the *S* wave are divided by the amplitude spectra of *P* waves in a 2-s time window before the *S* wave (Figure 8b). Spectral ratios for aftershocks (events 3, 4, 7, 13, 16, 18, and 23) occurring within the rupture zone show a maximum peak at 4–6 Hz at stations close to the fault trace, which decreases rapidly with the distance from the fault trace. In contrast, spectral ratios for aftershocks (events 5, 9, and12) occurring far away from the rupture zone show almost the same ratio at all stations of the array because they did not generate large-amplitude fault zone trapped waves. Figure 9 shows the spectral ratios versus distance from the main fault trace along array 1. On the basis of the distance exhibiting larger ratios, we estimated that the rupture zone at array 1 is ~100 m wide. The peak in spectral ratio in the fault zone is indicative of trapped wave energy while the flat curves show no such pattern. We have computed the spectral ratios for all aftershocks used in this study to determine which events occurred within the rupture zone and generated significant fault zone trapped waves.

[27] Figure 10a shows parallel-to-fault component seismograms recorded at array 1 for five aftershocks occurring (events 8, 10, 11, 17, and 20) occurring on the north LLF and another five aftershocks (events 4, 7, 14, 15, and 18) occurring on the more northerly directing line from the main shock epicenter at different depths and distances from the array. Locations of these events are shown in Figure 1. Prominent fault zone trapped waves were recorded for these aftershocks. Computed amplitude spectral ratios of trapped waves to *P* waves for these events show a maximum peak at 4–6 Hz appearing within the rupture zone. The delay time of trapped waves after *S* waves increases roughly with the hypocentral distance along the rupture zone. This effect is

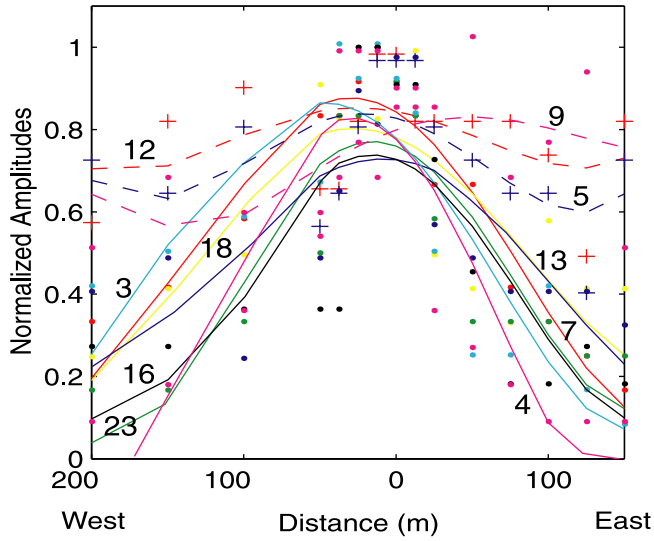

Figure 9. Computed amplitude spectral ratios at 15 stations of array 1 for 10 aftershocks versus distance from the main fault trace. Dots are the data points picked from spectral ratios in Figure 8b for events 3, 4, 7, 13, 16, 18, and 23 showing trapped waves, while crosses denote the data points for events 5, 9, and 12 without trapped waves. Curves are the fourth-order polynomial fit to the data for each event. Solid curves are for events showing trapped waves, while dashed curves are for events without trapped waves. Each curve is labeled by the event number.

shown more clearly in Figure 10b, in which the seismograms recorded at station ST0 for these events are plotted with the *S* waves aligned at 4 s. The delay time of dominant trapped waves after *S* waves increases from ~0.5 to ~2.0 s as the distance along the rupture zone increases from ~10 to 20 km, showing the existence of low-velocity waveguides on the north LLF and also on the more northerly line, respectively. We interpret that the low-velocity waveguide on the north LLF is partly resulted from dynamic rupture in the 1999 Hector Mine main shock. Thus we further interpret that a buried fault north on the main shock epicenter also ruptured in the Hector Mine event although it did not break to the surface. These observations suggest the bifurcation of the Hector Mine north rupture zone, consistent with our previous observations of trapped waves from aftershocks in 1999 (Figure 1) showing two subparallel rupture segments along the north LLF to west and along the more northerly buried fault to east in the northern rupture zone.

[28] However, we note that the increase of delay time is not linearly proportional to the increase of the distance due to the depth-dependent and lateral variations in velocity along the rupture zone as well as the location variation of the event off the principal slip plane. We also note that the delay time of trapped waves from events 4 and 17 (15–20 km north of array 1) did not increase with distance, suggesting that the low-velocity waveguides on the north LLF and the buried fault are well developed in a distance range of approximately 15 km north of the main shock epicenter.

[29] To the south of the Hector Mine rupture zone which had a more complicated pattern of surface breaks than that

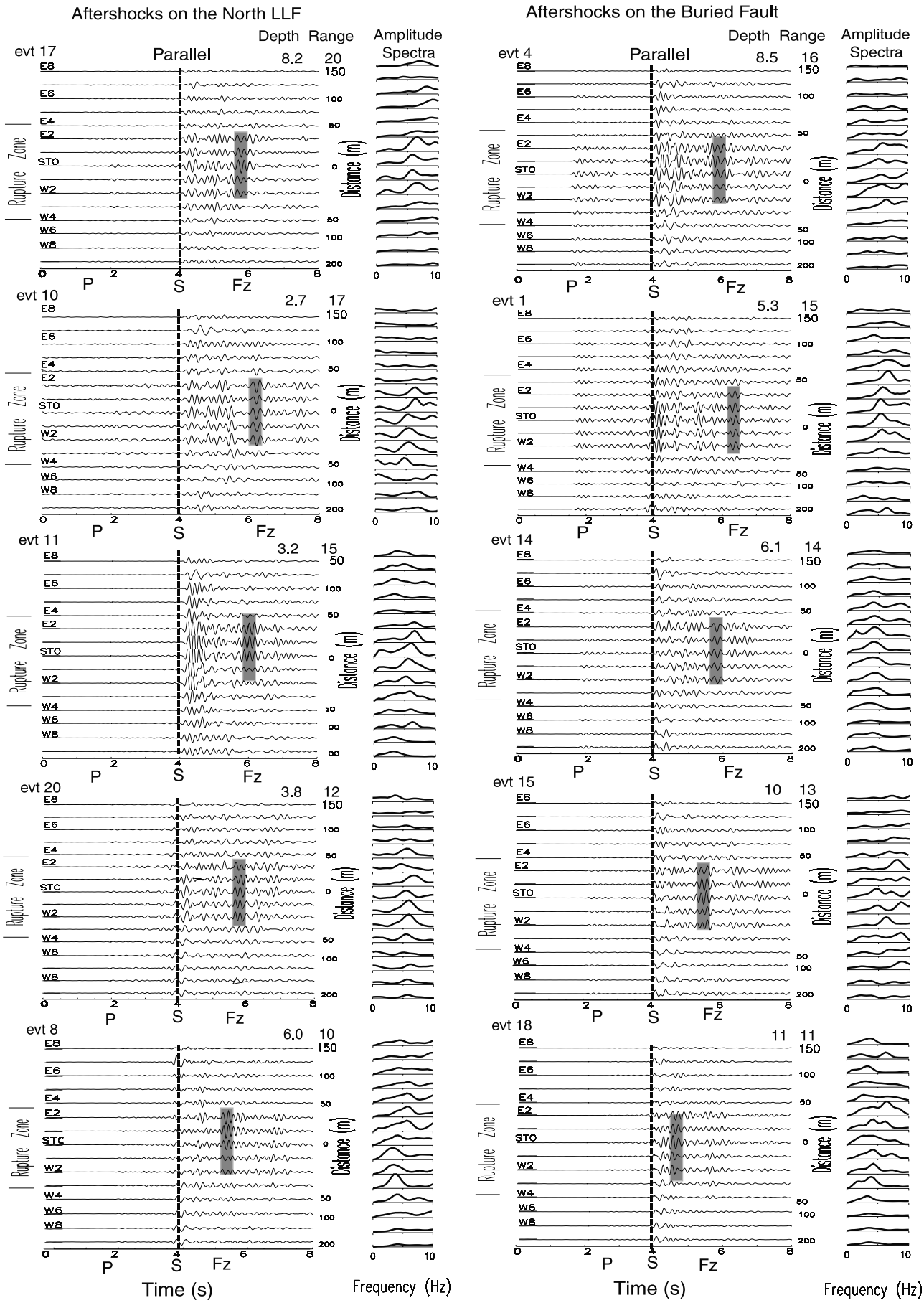
Aftershocks on the North LLF
Aftershocks on the Buried Fault
Depth Range
Amplitude Spectra
Parallel
evt 17
8.2 20
evt 10
2.7 17
evt 11
3.2 15
evt 20
3.8 12
evt 8
6.0 10
evt 4
8.5 16
evt 1
5.3 15
evt 14
6.1 14
evt 15
10 13
evt 18
11 11
E8
E6
E4
E2
STO
W2
W4
W6
W8
Rupture Zone
Distance (m)
P
S
Fz
Time (s)
Frequency (Hz)

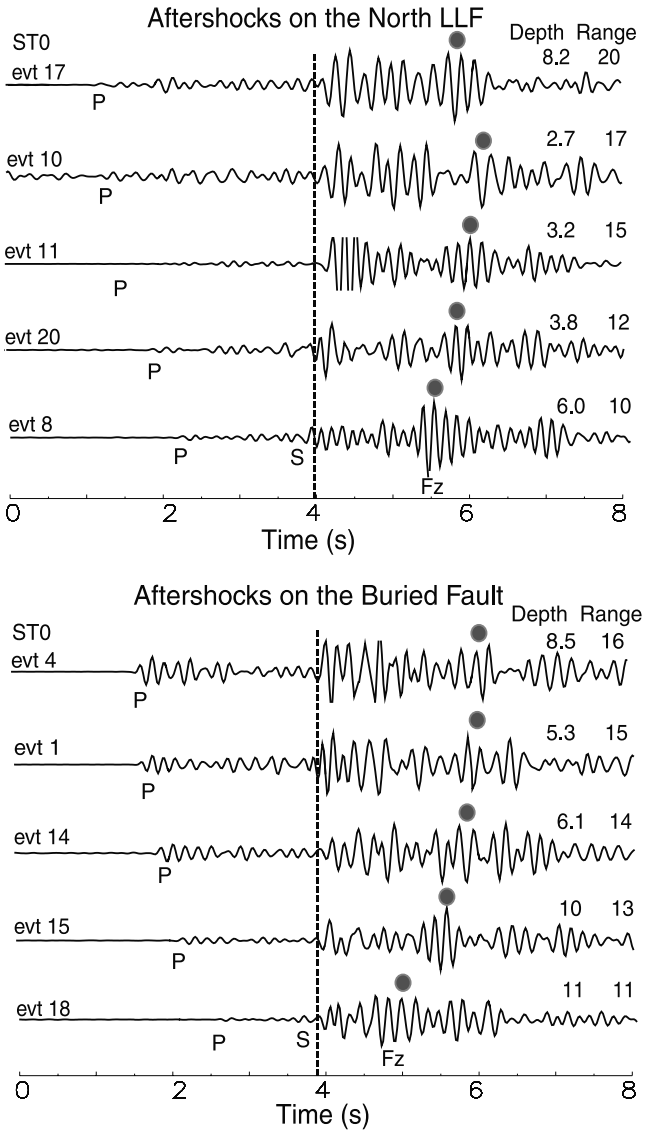

Figure 10b. Fault-parallel component seismograms at station ST0 of array 1 (top) for events 17, 10, 11, 20, and 8 occurring on the northwest LLF and (bottom) for events 4, 14, 15, 18, and 7 occurring on the buried fault. Seismograms are plotted with *S* arrivals aligned at 4 s. Shaded circles denote dominant trapped waves. The delay time of trapped waves after *S* arrivals approximately increases with the hypocentral distance of the events.

in the Bullion Mountains, we deployed arrays 2 and 3 across the surface slips on the south LLF and southeast BF in Bullion wash. Figure 11 shows seismograms recorded at the three arrays for three aftershocks (events 2, 13, and 23 in Figure 1) occurring within the rupture zone. Events 13 and 23 were located on the middle LLF, while event 2 was located near the south end of the LLF. Fault zone trapped waves appeared at arrays 1 and 3 but were not clear at array 2. The separation between the trapped waves and *S* waves for events 13 and 23 increases with distance between the event and array, again suggesting a roughly continuous low-velocity waveguide existing on the middle LLF. However, the delay time of trapped waves at array 3 for event 2 is smaller than that for event 13, although the two events occurred at the similar depths and event 2 had larger hypocentral distance than event 13 to the array. This indicates that the low-velocity waveguide on the LLF may not be well developed as it approaching the south end of the LLF where the rupture diminished. We also note a wave train after *S* wave, like trapped wave, appearing at stations on the east part of array 2 for the shallow event 2 and interpret these wave trains as surface waves due to soft sands in Bullion wash.

[30] Figure 12 shows seismograms recorded at three arrays for an aftershock (event 6) occurring near the southeast BF at 7.4 km depth and ~7 km southeast of array 2 (Figure 1). Trapped waves appeared at array 2 across the BF and array 1 across the north LLF, but not at array 3 across the south LLF. However, trapped modes at array 2 were not as dominant as those at array 1, indicating a weak trapping efficiency on the southeast BF than on the LLF. Seismograms recorded at array 2 for an aftershock (event 24 in Figure 1) occurring on the northwest BF, which did not rupture in the Hector Mine earthquake, show much shorter wave trains after *S* waves than those for event 6 although the distance from event 24 is larger than that from event 6. These observations suggest that the waveguide on the southeast BF is not developed as well as that on the LLF, but is softer than that on the northwest BF which did not rupture in the 1999 Hector Mine earthquake. The southeast BF dips to northeast and disconnects from the south LLF.

5. Finite Difference Simulations of Trapped Waves

[31] We have synthesized fault zone trapped waves recorded at the seismic array deployed across the Lavic Lake fault in the Bullion Mountains for the Hector Mine aftershocks in 1999 [*Li et al.*, 2002] using a 3-D finite difference code [*Graves*, 1996]. Simulations of these trapped waves resulted in a velocity and *Q* section across the LLF, which is applicable to first order to the structure of Hector Mine northern rupture segment in the Bullion Mountains.

[32] In the present paper, we first synthesize fault zone trapped waves generated by the near-surface explosions detonated in the rupture zone to document the shallow

Figure 10a. (opposite) Parallel-to-fault component seismograms recorded at array 1 for 10 Hector Mine aftershocks occurring at various depths and distances from the array. Right: Events 17, 10, 11, 20, and 8 occurred on the north LLF. (left) Events 4, 14, 15, 18, and 7 occurred on the buried fault. The depths and hypocentral distances (km) of aftershock are shown at the top right of each plot. Seismograms have been low pass filtered (<7 Hz) and are plotted using a fixed amplitude scale in each profile. *S* wave arrivals are aligned at 4 s. Fault zone trapped waves (Fz) marked by shaded bars are prominent at stations located within the rupture zone. Computed amplitude spectral ratios of trapped waves to *P* waves are plotted right to seismograms for each event.

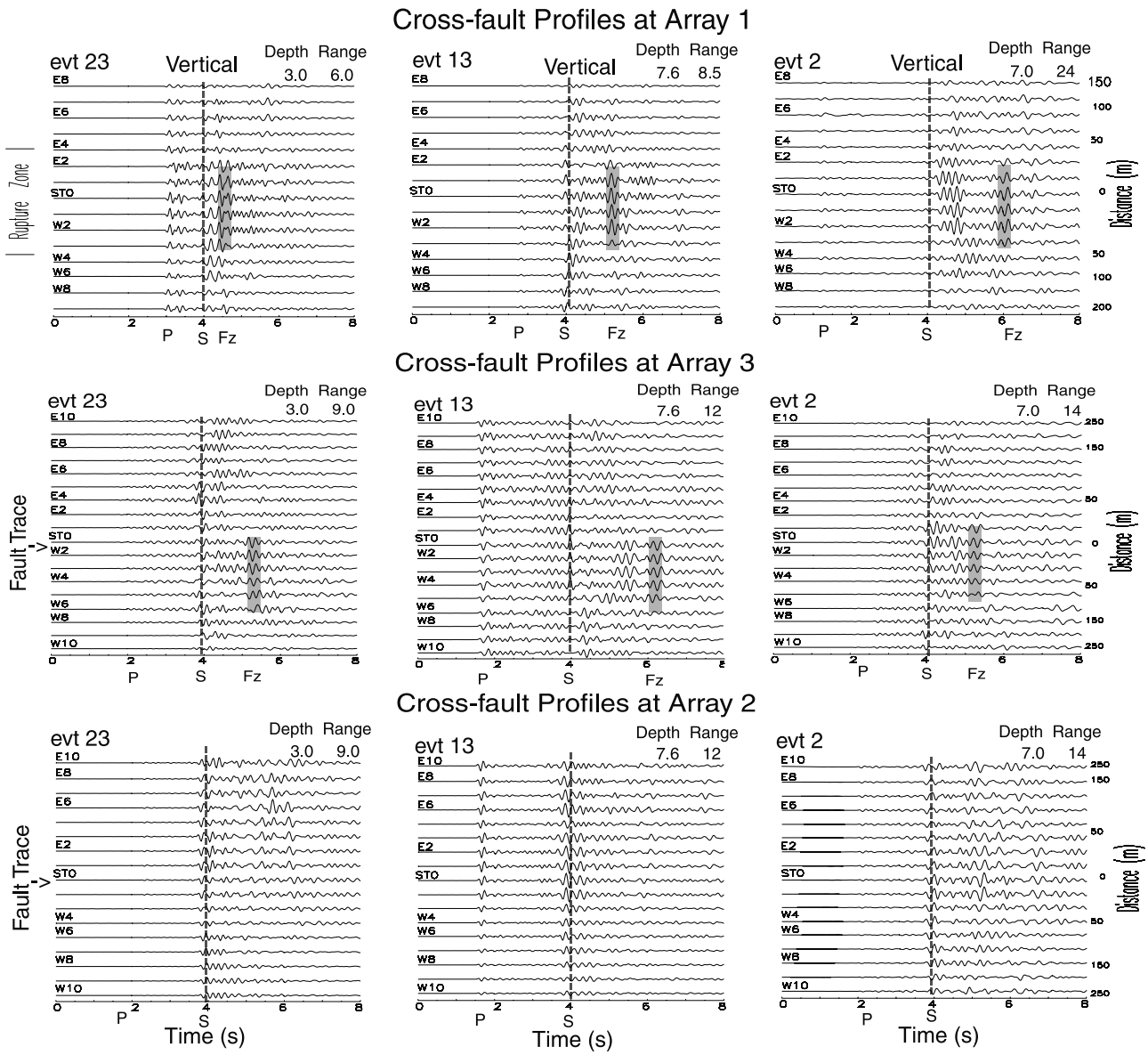

Figure 11. Vertical component seismograms recorded at arrays 1, 2, and 3 for three aftershocks (events 23, 13, and 2 in Figure 1 and Table 1). Events 23 and 13 occurred on the LLF in the Bullion Mountains, while event 2 occurred at the south end of the LLF. Shaded bars denote the prominent trapped waves after *S* waves.

structure of Hector Mine rupture zone to a depth of a few kilometers. This is interesting in its own right, but is most useful for stripping shallow effects to resolve internal rupture zone structure deeper, at the seismogenic depth. Then, we synthesize trapped waves from aftershocks. Combined with the results from trapped waves generated by explosions and aftershocks, we construct a model of the Hector Mine rupture zone with depth-variable structure in 3-D, including both northern and southern rupture segments. A well-imaged rupture zone structure will be helpful to localize and understand any postseismic changes in velocity along the faults ruptured in the 1999 *M*7.1 earthquake, should any be detected in our subsequent experiments.

[33] The 3-D finite difference computer code is second order in time and fourth order in space. It propagates the complete wave field through elastic media with a free-surface boundary and spatially variable anelastic damping (an approximate Q). The calculation used a 100-by-800-by-800 element grid in x-y-z coordinates with the grid spacing of 12.5 m to simulate a volume of 1.25 km in width, 10 km in length, and 10 km in depth. The grid volume was changed based on the distance and depth of the near-surface explosions and aftershocks to seismic arrays to minimize computer run time and memory. The fault zone waveguide is sandwiched between two quarter spaces, and placed down the middle of the grid. A explosion source was used for shots and double-couple sources for aftershocks. The source was placed within or close to the rupture zone.

[34] To find model parameters that best fit observed trapped waves, we tested various values for the fault zone

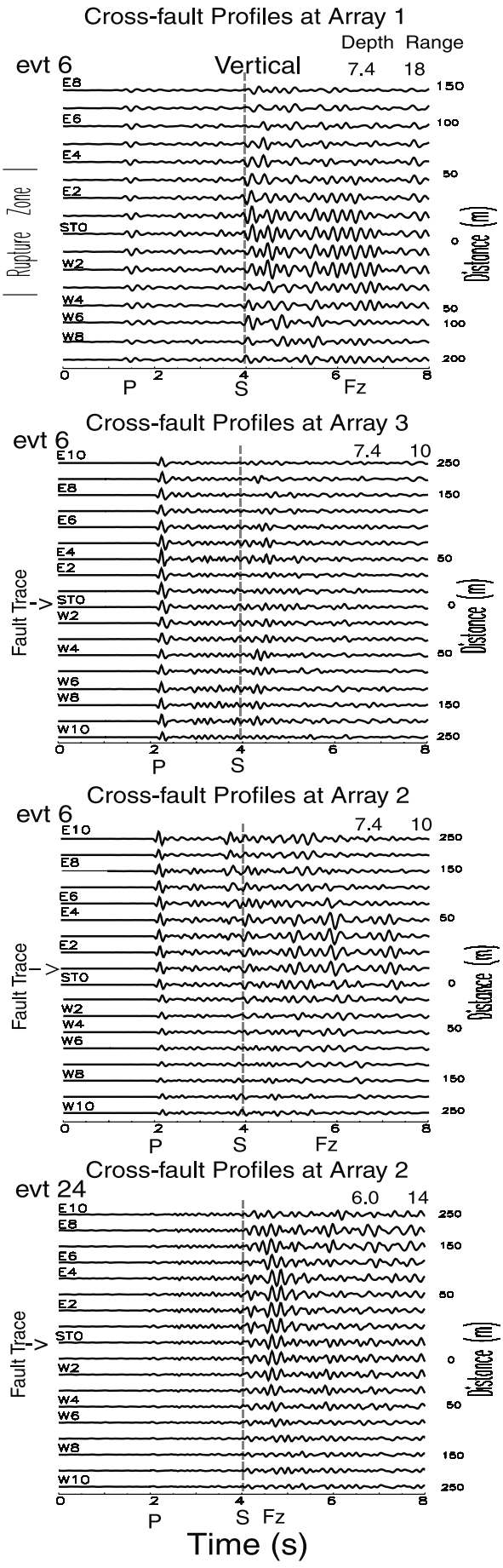

Table 2. Model Parameters for the Hector Mine Rupture Zone

Model Parameters	Best Fit					Test Range
	Layer 1	Layer 2	Layer 3	Layer 4	Layer 5	
Ruptures on the North LLF and Buried Fault in Bullion Mountains						
Depth of the layer, km	1.0	4.0	8.0	15.0		0.5 (step)
Waveguide width, m	100	100	75	75		50–150
Waveguide *S* velocity, km/s	1.0	1.6	2.1	2.5		0.5–3.0
Waveguide *P* velocity, km/s	2.2	3.6	4.2	4.4		1.5–5.0
Waveguide *Q* value	10	15	30	60		5–100
Wall rock *S* velocity, km/s	1.8	2.8	3.3	3.5		1.5–4.5
Wall rock *P* velocity, km/s	3.2	5.2	6.0	6.3		2.0–6.5
Wall rock *Q* value	20	30	60	100		10–200
Rupture on the Middle LLF in Quakenbush						
Depth of the layer, km	0.5	1.5	4.0	8.0	15.0	0.5 (step)
Waveguide width, m	100	100	75	75	75	50–150
Waveguide *S* velocity, km/s	0.7	1.1	1.8	2.1	2.5	0.5–3.0
Waveguide *P* velocity, km/s	1.6	2.2	3.6	4.2	4.4	1.5–5.0
Waveguide *Q* value	5	10	20	30	60	5–100
Wall rock *S* velocity, km/s	1.3	2.0	3.0	3.3	3.5	1.5–4.5
Wall rock *P* velocity, km/s	2.3	3.2	5.2	6.0	6.3	2.0–6.5
Wall rock *Q* value	10	20	30	60	100	10–200
Rupture on the South LLF Near Gypsum Ridge						
Depth of the layer, km	0.3	1.7	4.0	8.0	15.0	0.5 (step)
Waveguide width, m	100	100	75	75	75	50–150
Waveguide *S* velocity, km/s	0.8	1.3	2.0	2.5	2.7	0.5–3.0
Waveguide *P* velocity, km/s	1.6	2.2	3.6	4.2	4.4	1.5–5.0
Waveguide *Q* value	5	10	20	30	60	5–100
Wall rock *S* velocity, km/s	1.3	2.0	3.0	3.3	3.5	1.5–4.5
Wall rock *P* velocity, km/s	2.3	3.2	5.2	6.0	6.3	2.0–6.5
Wall rock *Q* value	10	20	30	60	100	10–200

width, velocity and *Q*, the wall rock velocity and *Q*, the layer depths, and the source location. The test range for each model parameter is shown in Table 2. In a modeling procedure, we changed the waveguide width by a step of 12.5 m (one grid), *S* velocity by 0.1 km/s, *P* velocity by

Figure 12. (opposite) Vertical component seismograms recorded at arrays 1, 2, and 3 for events 6 and 24 occurring on the southeast and northwest BF, respectively. Seismograms have been low pass filtered (<7 Hz) and are plotted using a fixed amplitude scale (the maximum peak-to-peak amplitude) in each profile. Trapped waves were registered at arrays 1 and 2 but not at array 3 for event 6.

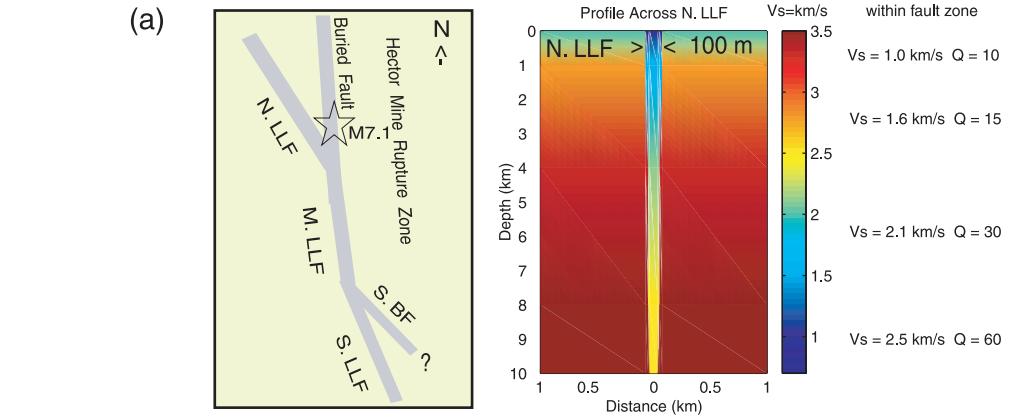
(a)
N
Buried Fault
Hector Mine Rupture Zone
N. LLF
M7.1
M. LLF
S. BF
S. LLF
?
Profile Across N. LLF
Vs=km/s
within fault zone
N. LLF > < 100 m
Depth (km)
Distance (km)
Vs = 1.0 km/s Q = 10
Vs = 1.6 km/s Q = 15
Vs = 2.1 km/s Q = 30
Vs = 2.5 km/s Q = 60

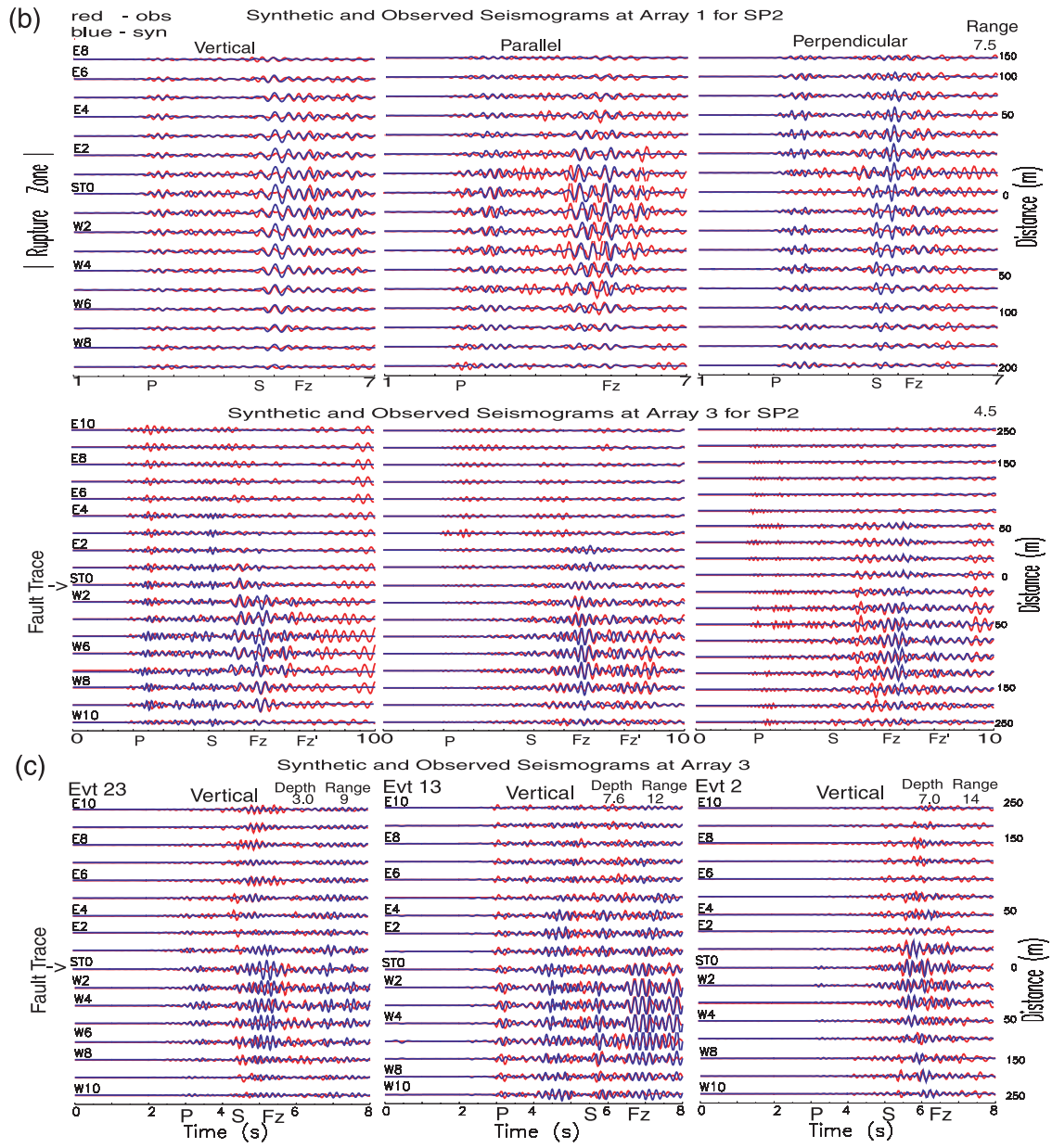
(b)
red - obs
blue - syn
Synthetic and Observed Seismograms at Array 1 for SP2
Vertical
Parallel
Perpendicular
Range
7.5
Rupture Zone
Distance (m)
Synthetic and Observed Seismograms at Array 3 for SP2
4.5
Fault Trace
(c)
Synthetic and Observed Seismograms at Array 3
Evt 23
Evt 13
Evt 2
Depth Range
3.0 9
7.6 12
7.0 14
Time (s)

0.2 km/s, and Q by 5 in the test ranges, respectively. When the fault zone width varies 25 m (two grids), or S velocity varies 0.2 km/s, or Q value varies 10, or source offset varies 25 m from the fault, or the fault zone depth is only a few kilometers for aftershocks at deeper levels, the amplitudes and dispersion of trapped waves change observably. In our previous paper for modeling of trapped waves at the Landers rupture zone [*Li et al.*, 1999, 2000], we have given the examples to show the sensitivity of synthetic trapped waveforms to these model parameters. In general, a wider fault zone produces trapped waves with lower dominant frequencies, and a slower fault zone produces longer dispersive wave trains of trapped waves. A lower Q fault zone produces trapped waves with smaller amplitudes and shorter wave trains at lower frequencies. A larger distance between the source and receiver produces a longer duration of trapped wave trains. A larger offset of the source location from the middle of the waveguide reduces the amplitude of trapped waves with respect to amplitudes of P and S waves. The variation of wall rock velocities and layer depths affects the arrival times of P and S waves, while the variation of wall rock Q produces minimal variation in modeling results.

[35] We have generated synthesized seismograms for explosions and a ftershocks in Table 1 using model parameters in Table 2 and Figure 13a. Figure 13b shows three-component synthetic seismograms in cross-fault profiles at array 1 for shot SP2 using model parameters for the north LLF in Table 2. Shot SP2 was located at the south front of the Bullion Mountains, ~7 km from the array. The synthetic and recorded seismograms have been filtered in frequency range of 2–6 Hz. Trapped waves are dominant between 4 and 7 s at stations within the rupture zone. The quality of fit of synthetics to observations is slightly different among three component seismograms, probably due to the affect of anisotropy which is not accounted in the present modeling. In the first-order significance, we obtained the best fit to explosion-generated seismograms at the north LLF using model parameters (Table 2 and Figure 13a): the top layer of the model is 100 m wide where the shear velocity is 1.0 km/s and Q is 10, while the second layer within the rupture zone has the shear velocity of 1.6 km/s and Q of 15. The velocities within the waveguide are reduced by ~35–45% from wall rock velocities.

[36] We further generated synthetic seismograms at array 3 for shot SP2. Array 3 was located ~5 km south of SP2 and across the LLF in Quakenbush where the basement rock was overlaid by alluvial and sedimentary rocks. We added a top layer with shear velocity of 0.65 km/s and Q of 5 within the rupture zone, and shear velocity of 1.3 km/s and Q of 10 for surrounding alluvium in the model used for the middle LLF (Table 2). Figure 13b also shows that synthetic trapped waves between 5 and 9 s are consistent with observations at array 3 for shot 2 although there is a mismatch in later wave trains for the vertical component. These simulation results show model parameters in Table 2 are applicable for the shallow portion of the Hector Mine rupture zone on the LLF.

[37] Then we combined the shallow structure of the rupture zone resolved from explosion-excited trapped waves with a depth-dependent model of the rupture zone in the Bullion Mountains, which has been obtained in our previous study using fault zone trapped waves [*Li et al.*, 2002]. We synthesized seismograms using a double-couple source in terms of this depth-dependent model to fit observations from the aftershocks occurring at different depths and hypocentral distances.

[38] For example, Figure 13c shows synthetic seismograms at array 3 for events 2, 13, and 23. Events 13 and 23 occurred on the middle LLF while event 2 occurred at the south end of the LLF. We used model parameters of the middle LLF for events 13 and 23, and model parameters of the south LLF for event 2 (Table 2). A double-couple source was located within the waveguide. We assumed strike and rake to be 0° and dip angle to be 90° for these events with small magnitudes, in accordance with the focal mechanisms of the large aftershocks given in the regional seismic network catalog. Using these angles for a double-couple source in our modeling showed a good result. In a first-order sense, synthetic waveforms are in agreement with the observations for these aftershocks, showing the validity of model parameters for the internal structure of the Hector Mine southern rupture zone.

[39] Figure 13 shows synthetic and observed seismograms at array 1 for four aftershocks (events 4, 13, 16, and 18 in Figure 1 and Table 1) occurring within the rupture zone in the Bullion Mountains. Event 13 was located at the depth of 7.6 km, and 3 km south of the array while event 18 was located at the 11 km depth and 3 km north of the array. The model parameters are given in Table 2 and Figure 13a. Tapped waves with relatively large amplitudes and long duration following S waves are concentrated within the rupture zone. Trapped waves from event 18 show longer duration of wave trains than those from event 13 because of

Figure 13. (opposite) (a) (left) Simplified geometry of the Hector Mine rupture zone. (right) Depth section of the rupture zone structural model across the north LLF. The fault zone is 100 m wide at the surface and tapered to 75 m at the depth of 10 km. Shear velocities and Q values within the waveguide are plotted at right to the model. Velocities and Q values increase with depth. Model parameters in the figure were used for generating synthetic seismograms best fit to observations. (b) The 3-D finite difference synthetic seismograms (blue lines) and observed (red lines) seismograms on the three-component profiles at arrays 1 and 3 for shot SP2 using the best fit model parameters in Table 2. An explosion source is located at the depth of 30 m and on the edge of the waveguide. Both synthetic and recorded seismograms have been filtered in 2–6 Hz and are plotted using a fixed amplitude scale in each plot. Trace spacings of synthetics are the same as field station spacings. Dead stations are not shown in profiles. (c) The 3-D finite difference synthetic and observed vertical component seismograms at array 3 for three aftershock (events 23, 13, and 2) occurring at different depths and distances from array. Model parameters for synthetic seismograms are given in Table 2. A double-couple source is located at the event depth and 50 m offset from the middle of the waveguide.

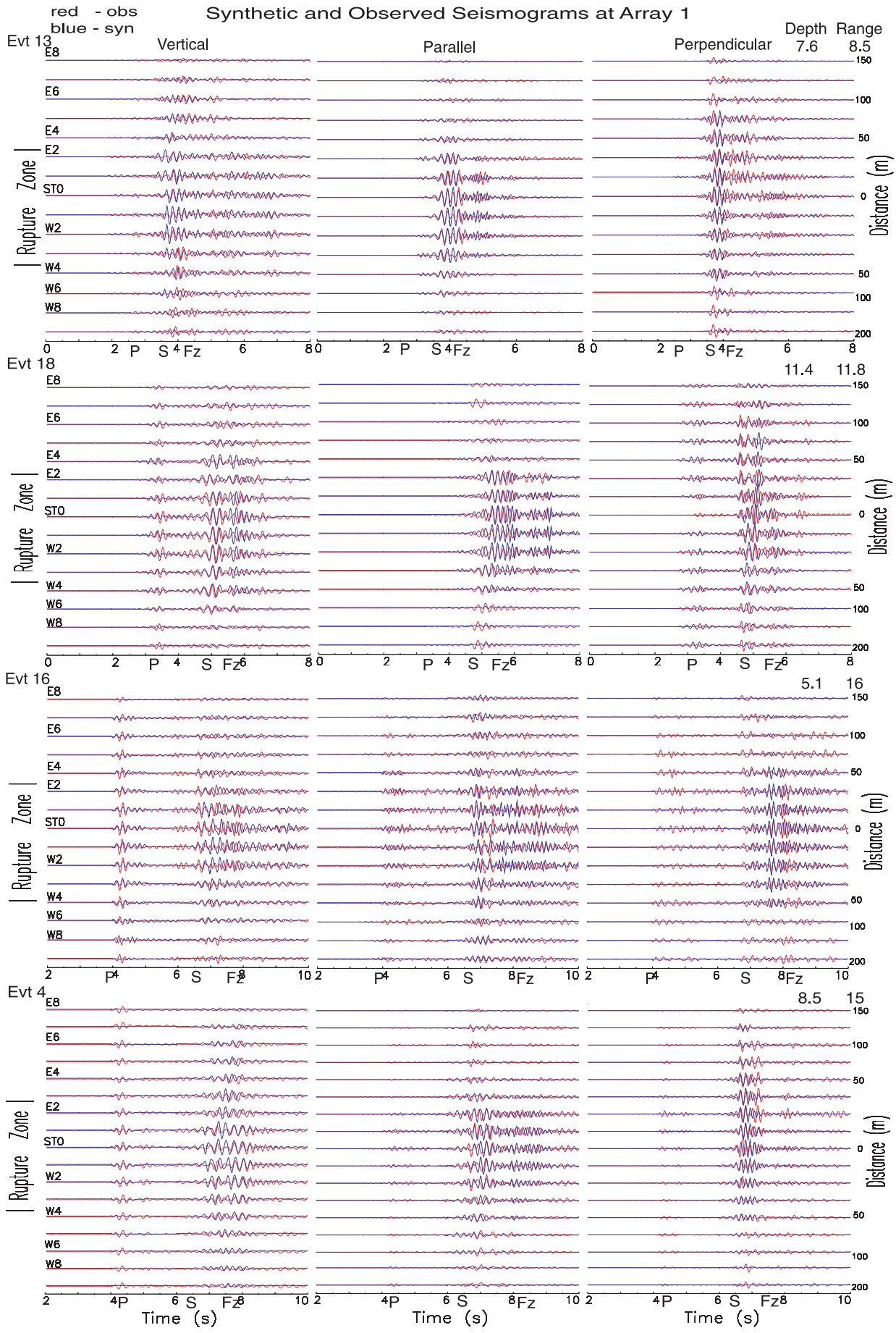
red - obs
blue - syn
Synthetic and Observed Seismograms at Array 1
Vertical
Parallel
Perpendicular
Depth Range
Evt 13
7.6 8.5
Evt 18
11.4 11.8
Evt 16
5.1 16
Evt 4
8.5 15
Rupture Zone
Distance (m)
E8
E6
E4
E2
ST0
W2
W4
W6
W8
P
S
Fz
Time (s)

the greater distance between event 18 and the array. We obtained a good agreement between synthetics and observations, showing that the model can explain the structure of the Hector Mine rupture zone at seismogenic depth. However, the fitness in three-component profiles are not the same, probably due to anisotropy near the fault. Our velocity model is for isotropic rocks.

[40] Events 16 and 4 occurred on the north LLF and the buried fault, respectively. We also obtained good fit of synthetic seismograms to observations using the same model parameters for them, showing that the low-velocity waveguide on the buried fault is similar to that on the north LLF (Figure 14).

[41] To match to *P* and *S* arrival times in modeling, we have changed hypocentral distances of events up to 0.5 km from the values given by catalogs, allowing for location error and also the lateral heterogeneity along the fault zone because they are not well constrained. We also note that synthetic *P* waves show smaller amplitudes than recorded *P* waves, while synthetic *S* and trapped waves match observations quite well, indicating that the waves might be scattered and disrupted by the heterogeneity (e.g., asperities, barriers, step overs, and multiple slip planes) within the rupture zone, which are not included in our model.

[42] The lateral variation in model parameters along the rupture zone at shallow depth is determined by simulations of exploration-generating trapped waves while the depth-dependent model structure mainly comes from trapped waves generated by aftershocks occurring at different depths. The model parameters in Table 2 are not unique because there is a trade-off among the parameters (e.g., the fault zone width, velocity contrast between the fault wall rocks, *Q* value, source location within the fault zone, and travel distance along the fault zone). This nonuniqueness problem and 3-D effects have been discussed in previous numerical studies for a delineation of fault zone structure using trapped waves [e.g., *Li and Leary*, 1990; *Leary et al.*, 1991; *Li and Vidale*, 1996; *Igel et al.*, 1997; *Ben-Zion*, 1998]. For instance, either increasing the waveguide width or decreasing the waveguide velocity in modeling will lower the dominant frequency of trapped waves. Low values of *Q* also affect considerably the dominant frequency and duration of trapped waves. The lower *Q* causes a shorter wave train of trapped waves at lower frequencies. The smaller velocity contrast between the waveguide and surrounding rocks also causes the shorter duration of trapped waves after *S* waves. Moving the source from the middle to the edge of the waveguide will reduce the amplitudes of trapped waves with respect to the *P* and *S* waves. However, the trade offs among the parameters can be reduced when we have estimates of some parameters to use as constraints in modeling, such as group velocities and *Q* values estimated from the dispersion and attenuation of trapped waves as well as *P* and *S* arrivals passing the wall rocks.

6. Dynamic Rupture Models

[43] The bifurcated geometry in the northern part of the Hector Mine fault is somewhat puzzling, because slip on one fault branch should relieve stress on the other. Upon a superficial analysis, the observation that the earthquake nucleated on the northerly branch (which did not rupture through to the surface) would imply that the rupture should not have jumped to the western (surface rupturing) LLF branch. However, the results of the present study and other studies strongly indicate that both segments ruptured in this earthquake. Therefore we have performed preliminary dynamic models to determine the circumstances under which rupture can jump to the LLF segment in the north. We are not attempting to match the detailed slip distribution pattern of this event but are rather investigating through simple models whether the rupture of both northern branches is consistent with basic rupture dynamics. More elaborate and detailed models are the subject of future work.

[44] The simplified fault geometry is shown in Figure 15a. For simplicity, and to isolate the effects of fault geometry, we assume a homogeneous half-space, with constant shear and normal stresses. We only consider the bifurcation of rupture in the north of the fault, and condense the southern segments to a single fault plane. We use the finite element method [*Whirley and Engelmann*, 1993; *Oglesby*, 1999], with computational and physical parameters given in Table 3. In our models, rupture is nucleated at a depth of 7.5 km, 4 km along strike from the branch point on the northern branch, consistent with the hypocentral location of *Scientists from USGS, SCEC, and CDMG* [2000]. We simulate cases in which the northern branch is allowed to rupture to the free surface, as well as cases in which the shear stress is set to zero in the upper 5 km of this branch, causing the rupture to die out in the shallow portion of the segment. A physical interpretation of this low-shear stress region is that it is due to the shallow part of the northern branch slipping in a previous event. Our physical situation is similar to that of *Aochi et al.* [2000], except that in the current method we explicitly model the variation of normal stress due to slip on segments with different orientation, and our nucleation takes place on one of the branch segments rather than on the stem segment.

Figure 14. (opposite) The 3-D finite difference synthetic and observed seismograms on the three-component cross-fault profiles at array 1 for four aftershocks (events 13, 18, 16, and 4) occurring within the rupture zone in the Bullion Mountains at different depths and distances. Events 13 and 18 were located south of the main shock epicenter, while events 16 and 4 were located on the north LLF and the buried fault, respectively. Model parameters for synthetic seismograms are given in Table 2. A double-couple is located at the event depths and 50 m offset from the middle of the waveguide. Both synthetic and recorded seismograms have been filtered in 2–6 Hz and are plotted using a fixed amplitude scale in each plot. Trace spacings of synthetics are the same as field station spacings. Dead traces for stations are not shown in profile. The origin time of the event is at 0 s.

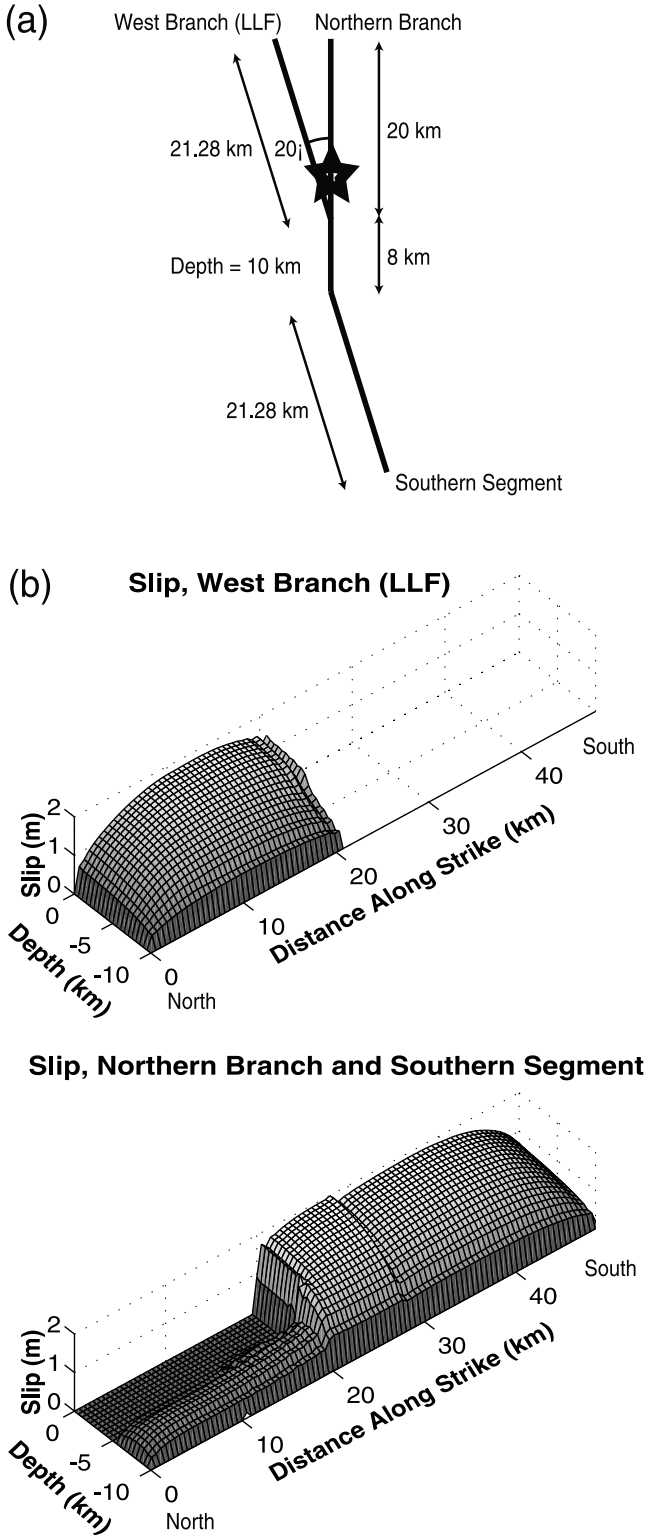

Figure 15. (a) Simplified fault geometry used in dynamic rupture simulations. The star denotes the hypocenter. (b) Fault slip in preferred fault model. Zero distance along strike corresponds to the northern part of the fault. Zero shear stress above 5 km depth on the northern branch causes rupture to die out in the northern branch, leading to slip on the west (LLF) branch. Note the kink in the slip distribution at the location of the change in strike (28 km) on the southern segment.

Table 3. Physical and Computational Parameters for Dynamic Models

Parameter	Value
Density	3000 kg/m^3
Shear modulus	3×10^5 bars
Poisson ratio	0.25
Initial shear stress	130 bars
Initial normal stress	200 bars
Static frictional coefficient	0.7
Sliding frictional coefficient	0.5
Critical slip-weakening distance	30 cm
Element size on fault	500 m $\times$ 500 m
Maximum calculated frequency	0.6 Hz

[45] The results indicate that the propagation of rupture to the LLF branch in the north of the fault is strongly aided when the rupture of the northern branch does not propagate to the surface, in keeping with observations. The slip from such a model is shown in Figure 15b. Slip initially accumulates only on the deep part of the northern branch, and dies out in the shallow part. As mentioned before, slip on this part of the northern segment relieves stress on the LLF segment (with a strong effect on both the shear and normal stresses on the LLF segment), but this is true only for overlapping regions of the faults. In nonoverlapping regions (i.e., the shallow part of the LLF), the effect on stress is the opposite: Slip on the northern segment brings the LLF closer to rupture. When slip reaches the junction between the northern and LLF segments, rupture can then jump to the LLF segment, accumulating the slip shown in Figure 15b. Note that slip is decreased on the deep part of the LLF segment near the segment junction, where the rupture inhibiting effect of the northern segment is the greatest. However, slip on the northern segment does not prevent the LLF segment from rupturing its entire depth. The surface slip on this branch is consistent with the slip mapped by *Scientists from USGS, SCEC, and CDMG* [2000]. The reversed directivity in our model is something that in principle could be tested with earthquake records.

[46] We have conducted enough tests with different stress configurations and hypocentral locations to indicate that the above results are insensitive to the precise tuning of the model. In particular, configurations in which the normal stress is higher on the LLF branch (consistent with a single tectonic stress field resolved on to both branches) also produce the above rupture pattern, as long as the shear stress is high enough to make rupture energetically favorable.

[47] Experiments with scenarios that allow the northern branch to rupture to the surface indicate that such configurations, in addition to being contrary to observations, are much less likely to allow rupture to jump to the LLF segment. The complete overlap between the fault segments causes the entire LLF segment to be brought farther from rupture by slip on the northern segment. In such models, even if some slip does occur on the LLF segment, it does not propagate out of a small subsurface patch. The physical reason that the northern segment did not rupture to the free surface is not elucidated by this study. In our preferred model, the low shear stress in the shallow part of the northern segment could be caused by an earlier event,

which would have relieved stress on this part of the fault. Alternatively, higher normal stress in this part of the fault could also have caused the rupture to die out there, as would a slip-hardening fault material. Further work may help to shed light on which physical mechanism is more consistent with observations.

7. Discussion and Conclusions

[48] We deployed portable seismometers in tight linear arrays across the Lavic Lake fault which ruptured in the *M*7.1 Hector Mine, California earthquake on 25 October 1999, to record fault zone trapped waves generated by explosions detonated within the rupture zone and aftershocks. Aftershocks located within the rupture zone produced 4–7 Hz fault zone trapped waves, while near-surface explosions produced 3–5 Hz trapped waves. The trapped waves were most prominent at stations close to the ruptured fault traces. The trapped waves recorded at the Hector Mine rupture zone are similar to those observed at the Landers rupture zone in 1992 [*Li et al.*, 1994a, 1994b, 1999, 2000] but peak at higher frequencies. The 3-D finite difference simulations of these trapped waves indicate a 75- to 100-m-wide low-velocity and low-Q waveguide along the Hector Mine rupture zone where the velocities are reduced by $\sim$35–45% from wall rock velocities, and Q is $\sim$10–60. Within the waveguide, S velocities vary from $\sim$1.0 km/s to $\sim$2.5 km/s in the depth range between the surface and $\sim$10 km. The rupture zone structure is not uniform with depth because the increasing pressure with increasing depth will strongly affect the crack density, fluid pressure, and amount of fluids, as well as the rate of healing of damage caused by earthquakes [*Sibson*, 1977; *Byerlee*, 1990; *Rice*, 1992]. It may also influence the development of fault gouge [*Scholz*, 1990; *Marone*, 1998a, 1998b] and the mineralogy of the rocks. For all these reasons, the fault zone properties are likely to be depth-dependent.

[49] We interpret that this distinct low-velocity waveguide mostly represents the process zone of inelastic deformation around the propagating crack tip in the 1999 Hector Mine earthquake, as is formed in theoretical work on existing fault zone rupture models [e.g., *Rice*, 1980; *Papageorgiou and Aki*, 1983; *Scholz*, 1990]. Although the low-velocity waveguide along the rupture surface probably also represents a wear zone that has accumulated over geological time, it is likely that the waveguide has been significantly weakened by the dynamic rupture in the most recent major earthquake. Repeated surveys using explosions at the Landers rupture zone have shown that the fault is healing (strengthening) after the 1992 *M*7.5 earthquake [*Li et al.*, 1998a; *Li and Vidale*, 2001], supporting a broken-then-healing cycle on the active fault.

[50] The reduction of velocities within the Hector Mine rupture zone is approximately the same as that within the Landers rupture zone [*Li et al.*, 2000], indicating that the fault zone rock was damaged to nearly the same degree in the two earthquakes. However, the waveguide width on the Hector Mine rupture zone is half that of the Landers rupture zone, roughly consistent with the proportional scaling of process zone size to rupture length as predicted in the published dynamic rupture model [e.g., *Cowie and Scholz*, 1992], although this model is appropriate for a single rupture on a simple slip plane. The partitioning between long-term and transient damage on the Hector Mine fault has not been evaluated yet but will be measured by repeated surveys in the following years.

[51] Locations of aftershocks showing fault zone trapped waves at the Hector Mine and Landers rupture zones revealed that multiple faults were involved in the Hector Mine and Landers earthquakes. At Landers, the rupture is segmented by step overs between preexisting faults [*Sieh et al.*, 1993; *Hauksson et al.*, 1993; *Li et al.*, 1994a, 1994b]. At Hector Mine, the northern rupture zone bifurcates along two subparallel fault strands; both of them extended approximately 15 km north of the main shock epicenter. The west slip plane of the northern rupture zone has surface expression, while the east slip plane is buried. This bifurcation is also suggested by aftershock locations [*Hauksson et al.*, 2000] and the study of the source process using strong motion, telemetry and surface deformation data [*Dreger and Kaverina*, 2000; *Simons et al.*, 2000]. Modeling of trapped waves from aftershocks occurring on the LLF and the buried fault shows that the waveguide parameters on the two rupture segments are similar, probably due to the similar slip displacement release on them in the main shock [*Ji et al.*, 2002].

[52] Although the current dynamic rupture simulations are quite simplified and do not attempt to match the specific moment release patterns of this event, they do show that very generic (not finely tuned) models can be made to produce the general features of the northern part of the rupture, including slip on both fault branches. The models indicate that the rupture of both northern branches is consistent with basic assumptions about the physics of the earthquake process. Future dynamic models will help to shed light on likely physical mechanisms for the lack of slip in the shallow northern segment, and will allow us to fit more precisely the slip and timing of rupture inferred from strong motion data. They may also shed light on the connection between the dynamic rupture process and the formation of the damage zone.

[53] In the south Hector Mine rupture zone, slip became smaller and more complicated in Quakenbush wash zone. The rupture on the south LLF passed the BF, and the slip diminished at a distance of $\sim$15 km south of the intersection between the LLF and BF. The rupture probably also extended a shorter distance along the southeast BF, which dips northeastward and disconnects from the LLF. We next plan to incorporate this complex fault geometry in 3-D dynamic simulations to understand why this particular set of faults slipped in the 1999 earthquake.

[54] **Acknowledgments.** This study was supported by NSF grant EAR-0001132 and the Southern California Earthquake Center. SCEC is funded by NSF Cooperative Agreement EAR-8920136 and USGS Cooperative Agreements 14-08-0001-A0899 and 1434-HQ-97AG01718. Special acknowledgments to the Marine Corps Air Ground Combat Center (MCAGCC), Twentynine Palms, California, for their permission to carry out the experiment on the base and their invaluable help when we deployed instruments in the Bullion Mountains. We thank L. Jones of the USGS for her coordination of our initial recording of trapped waves at the Hector Mine rupture zone and Karl Gross of the USGS for his coordination of our experiments in the Marine Base. Tom Burdette of the USGS detonated explosions. We thank Sarah Gonzalez, Chris Lynch, Rob Mellors, and Fei Xu for their work in the field experiment. We appreciate the support of IRIS-PASSCAL Instrument Center for the use of their instruments and Mark Alvarez for his collaboration in the experiment, as well as P. Davis for

the use of UCLA battery chargers. We thank Associated Editor Fred Pollitz, reviewer Ruth Harris, and an anonymous reviewer for their helpful comments on the manuscript. We also thank D. Dreger, B. Graves, H. Houston, K. Hudnut, S. Owen, P. Shearer, M. Simons, and F. Vernon for valuable discussions in this study. SCEC contribution 596.

References

Aki, K., Scaling law of earthquake source time-function, *Geophys. J. R. Astron. Soc.*, *31*, 3–25, 1972.

Aki, K., Asperities, barriers, characteristic earthquakes, and strong motion prediction, *J. Geophys. Res.*, *89*, 5867–5872, 1984.

Aochi, H., E. Fukuyama, and M. Matsu'ura, Selectivity of spontaneous rupture propagation on a branched fault, *Geophys. Res. Lett.*, *27*, 3635–3638, 2000.

Beck, S. L., and D. H. Christensen, Rupture process of the February 4, 1965, Rat Islands earthquake, *J. Geophys. Res.*, *96*, 2205–2221, 1991.

Ben-Zion, Y., Properties of seismic fault zone waves and their utility for imaging low-velocity structure, *J. Geophys. Res.*, *103*, 12,567–12,585, 1998.

Beroza, G. C., A. T. Cole, and W. L. Ellsworth, Stability of coda wave attenuation during the Loma Prieta, California, earthquake sequence, *J. Geophys. Res.*, *100*, 3977–3987, 1995.

Byerlee, J., Friction, overpressure and fault-normal compression, *Geophys. Res. Lett.*, *17*, 2109–2112, 1990.

Chester, F. M., J. P. Evans, and R. L. Biegel, Internal structure and weakening mechanisms of the San Andreas fault, *J. Geophys. Res.*, *98*, 771–786, 1993.

Cowie, P. A., and C. H. Scholz, Growth of faults by accumulation of seismic slip, *J. Geophys. Res.*, *97*, 11,085–11,095, 1992.

Das, S., and K. Aki, Fault plane with barriers: A versatile earthquake model, *J. Geophys. Res.*, *82*, 5658–5670, 1977.

Day, S. M., Three-dimensional simulation of spontaneous rupture: The effect of nonuniform prestress, *Bull. Seismol. Soc. Am.*, *72*, 1881–1902, 1982.

Dieterich, J. H., Time-dependent friction and the mechanics of strike-slip, *Pure Appl. Geophys.*, *116*, 790–806, 1978.

Dreger, D., and A. Kaverina, Seismic remote sensing for the earthquake source process and near-source strong shaking: A case study of the October 16, 1999 Hector Mine earthquake, *Geophys. Res. Lett.*, *27*, 1941–1944, 2000.

Graves, R. W., Simulating seismic wave propagation in 3D elastic media using staggered-grid finite differences, *Bull. Seismol. Soc. Am.*, *86*, 1091–1106, 1996.

Harris, R. A., and S. M. Day, Dynamics of fault interaction: Parallel strike-slip faults, *J. Geophys. Res.*, *98*, 4461–4472, 1993.

Harris, R. A., and S. M. Day, Dynamic 3D simulations of earthquakes on en echelon faults, *Geophys. Res. Lett.*, *26*, 2089–2092, 1999.

Hauksson, E., L. Jones, K. Hutton, and D. Eberhart-Phillips, The 1992 Landers earthquake sequence: Seismological observations, *J. Geophys. Res.*, *98*, 19,835–19,858, 1993.

Hauksson, E., K. Hutton, and L. Jones, Seismotectonicsof the 1999 *Mw*7.1 Hector Mine earthquake sequence, southern California, paper presented at SCEC Annual Meeting at Oxnard, Calif., 17–20, 2000.

Hough, S. E., Y. Ben-Zion, and P. Leary, Fault-zone waves observed at the southern Joshua Tree earthquake rupture zone, *Bull. Seismol. Soc. Am.*, *84*, 761–767, 1994.

Igel, H., Y. Ben-Zion, and P. Leary, Simulation of *SH* and *P-SV* wave propagation in fault zone, *Geophys. J. Int.*, *128*, 533–546, 1997.

Ji, C., D. J. Wald, and D. V. Helmberger, Source description of the 1999 Hector Mine, California earthquake, part II, Complexity of slip history, *Bull. Seismol. Soc. Am.*, *92*, 1208–1226, 2002.

Jongmans, D., and P. E. Malin, Microearthquake *S*-wave observations from 0 to 1 km in the Varian Well at Parkfield, California, *Bull. Seismol. Soc. Am.*, *85*, 1805–1820, 1995.

Kanamori, H., Mechanics of earthquakes, *Annu. Rev. Earth Planet. Science*, *22*, 207–237, 1994.

Kranz, R. L., and C. H. Scholz, Critical dilatant volume of rocks at the onset of Tertiary creep, *J. Geophys. Res.*, *82*, 4893–4895, 1977.

Leary, P. C., H. Igel, and Y. Ben-Zion, Observation and modeling of fault zone seismic trapped waves in aid of precise precursory microearthquake location and evaluation, paper presented at Conference on Earthquake Prediction: State-of-the Art, Strasbourg, France, 15–18 Oct. 1991.

Lees, J. M., and P. E. Malin, Tomographic images of *P* wave velocity variation at Parkfield, California, *J. Geophys. Res.*, *95*, 21,793–21,804, 1990.

Li, Y. G., Trapped modes in a transversely isotropic fault-zone, Ph.D. thesis, pp. 168–189, Univ. of South. Calif., Los Angeles, 1988.

Li, Y. G., and P. C. Leary, Fault-zone trapped seismic waves, *Bull. Seismol. Soc. Am.*, *80*, 1245–1271, 1990.

Li, Y. G., and J. E. Vidale, Low-velocity fault-zone guided waves: Numerical investigations of trapping efficiency, *Bull. Seismol. Soc. Am.*, *86*, 371–378, 1996.

Li, Y. G., and J. E. Vidale, Healing of the shallow fault zone from 1994–1998 after the 1992 *M*7.5 Landers, California, earthquake, *Geophys. Res. Lett.*, *28*, 2999–3002, 2001.

Li, Y. G., P. C. Leary, K. Aki, and P. E. Malin, Seismic trapped modes in the Oroville and San Andreas fault zones, *Science*, *249*, 763–766, 1990.

Li, Y. G., K. Aki, D. Adams, A. Hasemi, and W. H. K. Lee, Seismic guided waves trapped in the fault zone of the Landers, California, earthquake of 1992, *J. Geophys. Res.*, *99*, 11,705–11,722, 1994a.

Li, Y. G., J. E. Vidale, K. Aki, C. J. Marone, and W. H. K. Lee, Fine structure of the Landers fault zone: Segmentation and the rupture process, *Science*, *256*, 367–370, 1994b.

Li, Y. G., F. L. Vernon, and K. Aki, San Jacinto fault-zone guided waves: A discrimination for recently active fault strands near Anza, California, *J. Geophys. Res.*, *102*, 11,689–11,701, 1997a.

Li, Y. G., W. L. Ellsworth, C. H. Thurber, P. E. Malin, and K. Aki, Fault-zone guided waves from explosions in the San Andreas fault at Parkfield and Cienega Valley, California, *Bull. Seismol. Soc. Am.*, *87*, 1–15, 1997b.

Li, Y. G., J. E. Vidale, K. Aki, F. Xu, and T. Burdette, Evidence of shallow fault zone strengthening after the 1992 *M*7.5 Landers, California, earthquake, *Science*, *279*, 217–219, 1998a.

Li, Y. G., K. Aki, J. E. Vidale, and M. G. Alvarez, A delineation of the Nojima fault ruptured in the *M*7.2 Kobe, Japan, earthquake of 1995 using fault-zone trapped waves, *J. Geophys. Res.*, *103*, 7247–7263, 1998b.

Li, Y. G., K. Aki, J. E. Vidale, and F. Xu, Shallow structure of the Landers fault zone from explosion-generated trapped waves, *J. Geophys. Res.*, *104*, 20,257–20,275, 1999.

Li, Y. G., J. E. Vidale, and K. Aki, Depth-dependent structure of the Landers fault zone using fault zone trapped waves generated by aftershocks, *J. Geophys. Res.*, *105*, 6237–6254, 2000.

Li, Y. G., J. E. Vidale, S. M. Day, and D. D. Oglesby, Study of the *M*7.1 Hector Mine, California, earthquake fault plan by fault-zone trapped waves, *Bull. Seismol. Soc. Am.*, *92*, 1318–1332, 2002.

Malin, P. E., S. N. Blakeslee, M. G. Alvarez, and A. J. Martin, Microearthquake imaging of the Parkfield asperity, *Science*, *244*, 557–559, 1989.

Marone, C., Laboratory-derived friction laws and their application to seismic faulting, *Annu. Rev. Earth Planet. Sci.*, *26*, 643–696, 1998a.

Marone, C., The effect of loading rate on static friction and the rate of fault healing during the earthquake cycle, *Nature*, *391*, 69–72, 1998b.

Michael, A. J., and D. M. Eberhart-Phillips, Relations among fault behavior, subsurface geology, and three-dimensional velocity models, *Science*, *253*, 651–654, 1991.

Michelini, A., and T. V. McEvilly, Seismological studies at Parkfield, I, Simultaneous inversion for velocity structure and hypocenters using cubic B-splines parameterization, *Bull. Seismol. Soc. Am.*, *81*, 524–552, 1991.

Mooney, W. D., and A. Ginzburg, Seismic measurements of the internal properties of fault zones, *Pure Appl. Geophys.*, *124*, 141–157, 1986.

Oglesby, D. D., Earthquake dynamics on dip-slip faults, Ph.D. thesis, Univ. of Calif., Santa Barbara, 1999.

Papageorgiou, A. S., and K. Aki, A specific barrier model for the quantitative description of inhomogeneous faulting and the prediction of strong motion, I, Description of the model, *Bull. Seismol. Soc. Am.*, *73*, 693–722, 1983.

Peltzer, G., P. Rosen, F. Rogez, and K. Hudnut, Poroelastic rebound along the Landers 1992 earthquake surface rupture, *J. Geophys. Res.*, *103*, 30,131–30,145, 1998.

Rice, J. R., The mechanics of earthquake rupture, in *Physics of the Earth's Interior*, edited by A. M. Dziewonski and E. Boschi, pp. 555–649, North-Holland, New York, 1980.

Rice, J. R., Fault stress states, pore pressure distributions, and the weakness of the San Andreas fault, in *Fault Mechanics and Transport Properties of Rocks*, edited by B. Evans and T.-F. Wong, pp. 475–503, Academic, San Diego, Calif., 1992.

Scholz, C. H., *The Mechanics of Earthquakes and Faulting*, Cambridge Univ. Press, New York, 1990.

Schwartz, D. P., and K. J. Coppersmith, Fault behavior and characteristic earthquakes: Examples from the Wasatch and Andreas fault zones, *J. Geophys. Res.*, *89*, 5681–5698, 1984.

Scientists from the USGS, SCEC, and CDMG, Preliminary report on the 16 October 1999 *M*7.1 Hector Mine, California, earthquake, *Seismol. Res. Lett.*, *71*, 11–23, 2000.

Sibson, R. H., Fault rocks and fault mechanisms, *J. Geol. Soc. London*, *133*, 191–213, 1977.

Sibson, R. H., Stopping of earthquake ruptures at dilational fault jogs, *Nature*, *316*, 248–251, 1985.

Sieh, K., et al., Near-field investigations of the Landers earthquake sequence, April to July 1992, *Science*, *260*, 171–176, 1993.

Simons, M., Y. Fialko, C. Ji, and L. Rivera, Co-seismic static deformation from the October 16, 1999 *M*7.1 Hector Mine CA earthquake, *Eos Trans. AGU*, *81*(48), Fall Meet. Suppl., Abstract S61A-03, 2000.

Thurber, C. H., S. Roecker, W. Ellsworth, Y. Chen, W. Lutter, and R. Sessions, Two-dimensional seismic image of the San Andreas fault in the northern Gabilan Range, central California: Evidence for fluids in the fault zone, *Geophys. Res. Lett.*, *24*, 1591–1594, 1997.

Vidale, J. E., W. L. Ellsworth, A. Cole, and C. Marone, Rupture variation with recurrence interval in eighteen cycles of a small earthquake, *Nature*, *368*, 624–626, 1994.

Wald, D. J., and T. H. Heaton, Spatial and temporal distribution of slip for the 1992 Landers, California, earthquake, *Bull. Seismol. Soc. Am.*, *84*, 668–691, 1994.

Wesnousky, S. G., Earthquakes, quaternary faults, and seismic hazard in California, *J. Geophys. Res.*, *91*, 12,587–12,631, 2000.

Wesson, R. L., and W. L. Ellsworth, Seismicity preceding moderate earthquakes in California, *J. Geophys. Res.*, *78*, 8527–8545, 1973.

Whirley, R. G., and B. E. Engelmann, DYNA3D: A nonlinear, explicit, three-dimensional finite element code for solid and structural mechanics – User manual, *UCRL-MA-11,07254 Rev. 1.*, Univ. of Calif., Lawrence Livermore Natl. Lab., Livermore, Calif., 1993.

Working Group on California Earthquake Probabilities, Seismic hazards in southern California: Probable earthquakes, 1994 to 2004, *Bull. Seismol. Soc. Am.*, *85*, 397–439, 1995.

E. Cochran and J. E. Vidale, Department of Earth and Space Sciences, University of California, Los Angeles, CA 90095, USA. (vidale@moho.ess.ucla.edu)

S. M. Day, Department of Geological Sciences, San Diego State University, San Diego, CA 92182, USA. (day@moho.sdsu.edu)

Y.-G. Li, Department of Earth Sciences, University of Southern California, Los Angeles, CA 90089-0740, USA. (ygli@terra.usc.edu)

D. D. Oglesby, Department of Earth Sciences, University of Riverside, Riverside, CA 92521, USA. (doglesby@namazu.ucr.edu)